

Inward-Growing Self-Assembly of Inverse Opal Deep UV Wavelength-Selecting Device

by

Thomas J. Deering

B.S., Chemistry, State University of New York at Buffalo, 2017

Submitted to the Graduate Faculty of the
Dietrich School of Arts and Sciences in partial fulfillment
of the requirements for the degree of
Master of Science

University of Pittsburgh

2020

UNIVERSITY OF PITTSBURGH

DIETRICH SCHOOL OF ARTS AND SCIENCES

This thesis was presented

by

Thomas J. Deering

It was defended on

March 27, 2020

and approved by

Dr. Haitao Liu, Associate Professor, Department of Chemistry, University of Pittsburgh

Dr. David Waldeck, Professor, Department of Chemistry, University of Pittsburgh

Thesis Advisor: Dr. Sanford Asher, Distinguished Professor, Department of Chemistry,
University of Pittsburgh

Copyright © by Thomas J. Deering

2020

Inward-Growing Self-Assembly of Inverse Opal Deep UV Wavelength-Selecting Device

Thomas J. Deering, MS

University of Pittsburgh, 2020

Photonic crystals (PhCs) are materials which use spatial modulations in their refractive index to affect the propagation of light. PhCs possess photonic stopbands, at which significant amounts of light of particular wavelengths are Bragg diffracted. The diffraction properties of PhCs have previously been utilized for wavelength-selecting devices (WSDs) for spectrometers. Previous PhC-based WSDs consisted of particles suspended in water, and therefore were not mechanically robust, while solid WSDs diffusely scattered most of the incident light. Therefore, we developed the inward-growing co-assembly method to fabricate solid deep UV-diffracting PhCs with low diffuse scattering.

We self-assembled polystyrene nanoparticles (PSNPs) on a horizontal substrate while sol-gel reactions of a silicate precursor formed an ordered network of silica around the PSNPs. Removing the PSNPs by dissolution in tetrahydrofuran (THF) and piranha solution yielded an inverse opal (IO) consisting of an ordered array of air voids surrounded by the silica network. This IO diffracts deep UV light with much less diffuse scattering than previously-published deep UV-diffracting IOs. Scanning electron microscopy (SEM) shows that removing the PSNPs using THF and piranha solution does not deform the silica network to the same extent as other methods like calcination. The diffraction band of these IOs is narrower and more intense than our group's previously-published deep UV-diffracting IO, and the diffuse scattering is much lower. Further optimization of this method could produce WSDs that are sufficiently selective for use in deep UV spectrometers.

Table of Contents

1.0 Introduction.....	1
1.1 Background.....	1
1.1.1 Photonic Crystals.....	1
1.1.2 Colloidal Crystals.....	3
1.1.3 Deep UV Resonance Raman Spectroscopy of Explosives.....	5
1.2 Prior Work.....	7
1.2.1 Development of CCA Deep UV WSDs.....	7
1.2.2 Development of IO Deep UV WSDs.....	8
2.0 Experimental.....	11
2.1 Horizontal Co-Assembly Procedure.....	11
2.1.1 Substrate Preparation.....	11
2.1.2 Colloidal Suspension Preparation.....	11
2.1.3 Preparation of PS/SiO₂ Photonic Crystals.....	12
2.2 Inverse Opal Fabrication.....	12
2.3 Characterization of Stopband Properties.....	13
2.4 Measurement of Structural Dimensions.....	13
2.5 Filling Inverse Opal Voids with Water.....	14
3.0 Development of Inward-Growing Co-Assembly of Polystyrene/Silica Photonic Crystals.....	15
3.1 Motivation.....	15
3.2 Mechanism of Inward-Growing Co-Assembly.....	16

3.3 Optimization of Fabrication Conditions	18
3.3.1 Optimization of Environmental Conditions	19
3.3.2 Optimization of PSNP Volume Fraction	19
3.3.3 Optimization of TEOS Solution Volume Fraction.....	21
3.3.4 Optimization of HCl Concentration.....	22
4.0 Fabrication of Deep UV-Diffracting Silica Inverse Opals.....	26
4.1 Removal of PSNPs from PS/SiO₂ Photonic Crystals.....	26
4.2 Robustness of the Silica Network	27
4.2.1 Robustness at the Time of PSNP Removal	27
4.2.2 Robustness Following Removal	31
5.0 Silica Inverse Opal Diffraction Properties	35
5.1 Effects of Disorder	35
5.2 Diffraction Bandwidth	37
6.0 Conclusions and Future Work.....	40
Appendix A Synthesis of PSNPs	42
Bibliography	44

List of Tables

Table 1. Effect of IO fabrication method on compression of the silica network.....	30
---	-----------

List of Figures

Figure 1. Bragg diffraction by a PhC.....	2
Figure 2. Graphic representations of various types of colloidal crystals.....	3
Figure 3. Chemical structures and molar absorptivities of some common explosives.	6
Figure 4. Hydrolysis and condensation of TEOS to form silica.	8
Figure 5. Characterization of inverse opals fabricated by vertical co-assembly.	9
Figure 6. Optical profilometry image of the corner of a PS/SiO₂ PhC fabricated by inward-growing co-assembly of PSNPs and TEOS.....	17
Figure 7. Determination of the optimal PSNP volume fraction.....	20
Figure 8. PS/SiO₂ PhCs fabricated with varying volume fractions of TEOS solution in the initial suspension.	22
Figure 9. Dominant protonation states of species relevant to co-assembly as a function of pH.	23
Figure 10. Effect of pH on the formation of robust silica networks.	25
Figure 11. Comparison of extinction spectra of an inverse opal fabricated by THF/piranha treatment before and after calcination at 500°C.....	29
Figure 12. Side-profile SEM images of silica IOs fabricated by (a) calcination at 500°C and (b) THF/piranha solvent-based treatment.....	30
Figure 13. Comparison of extinction spectra from the same region of the same IO sample recorded immediately upon PSNP removal (black) and 28 days following PSNP removal (red).	32

Figure 14. The effect of heating TEOS solution prior to inward-growing co-assembly on the change in stopband wavelength observed 3 weeks following fabrication..... 34

Figure 15. Comparison of extinction spectra of silica inverse opals fabricated by (a) vertical co-assembly and (b) inward-growing co-assembly. 36

Figure 16. Normal-incidence extinction spectra of an IO in air (black), water (red), and after removing the water (green). 39

List of Equations

Equation 1.....	1
Equation 2.....	2
Equation 3.....	10

1.0 Introduction

1.1 Background

1.1.1 Photonic Crystals

Photonic crystals (PhCs) are materials that possess spatial modulations in refractive index that affect the propagation of light through these materials. This modulation in refractive index is achieved by periodic alternations between one material and another, which can be periodic in one, two, or three dimensions. Such structures are known as 1D, 2D, and 3D PhCs, respectively. These materials can be in any state of matter, and many PhCs consist of alternating regions of solid material and air. The ways in which light propagation is affected by PhCs are roughly analogous to the effects of atomic crystals on x-rays, but on length scales ~ 3 orders of magnitude larger. As light interacts with these materials, it either scatters in such a way that it constructively or destructively interferes, or propagates through the crystal. In particular, for 3D PhCs, a relatively strong constructive interference known as Bragg diffraction occurs when the Bragg-Snell Law is satisfied.¹ (Equation 1, Figure 1)

$$m\lambda = 2D \sqrt{n_{eff}^2 - \sin^2\theta} \quad \text{Equation 1}$$

As seen in Equation 1, the diffracted wavelength (λ) for a particular diffraction order (m) depends on the spacing of the diffracting planes (D), the effective refractive index of the PhC (n_{eff}), and the angle between the incident light and the PhC normal (θ). The effective refractive index of

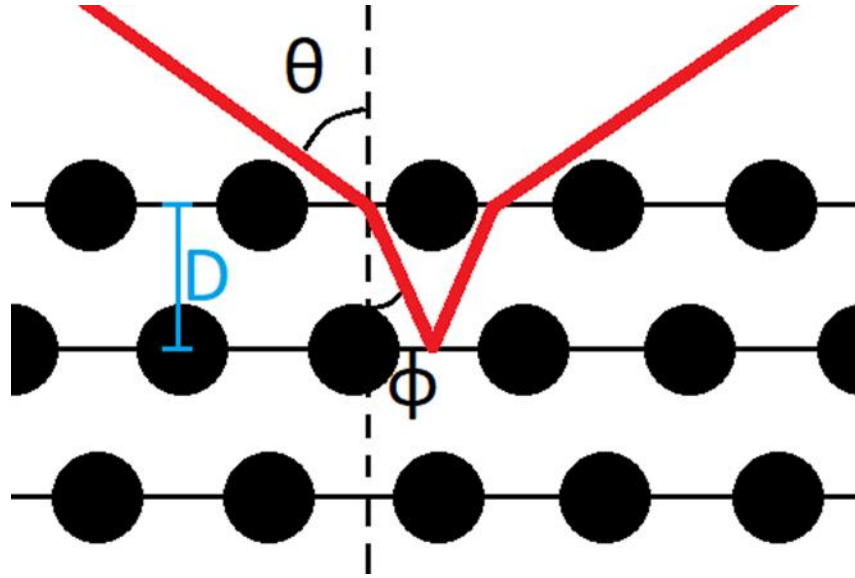


Figure 1. Bragg diffraction by a PhC. Incident light approaches the PhC at an angle θ relative to the normal of the PhC. Upon entering the PhC, the light within the PhC is refracted to a different angle ϕ . Light at the wavelength fitting the Bragg-Snell Law (Equation 1) diffracts from each of the diffracting planes (the centers of which are separated by a distance D). Other wavelengths will propagate through the PhC.

a PhC is a weighted average of the refractive indices of the constituent materials of the PhC, based on their volume fractions (f).² (Equation 2)

$$n_{eff} = \sqrt{\sum_i n_i^2 f_i} \quad \text{Equation 2}$$

The Bragg-Snell Law is so called because it combines Bragg's Law, typically used to describe x-ray diffraction, with Snell's Law to account for refraction by the PhC. In practice, the Bragg-Snell Law defines the center of a distribution of wavelengths diffracted by the PhC, known as the stopband. The intensity of the stopband is known to decrease, and the diffraction bandwidth increases, with increased disorder (i.e. greater deviation from perfect crystalline packing). Additionally, increasing the refractive index contrast between the constituent materials of the PhC increases both the diffraction intensity and bandwidth.³ If the refractive index contrast is

sufficiently high, a full photonic band gap occurs, at which no photons of a particular wavelength propagate through the PhC.^{4,5}

1.1.2 Colloidal Crystals

Colloidal crystals, which consist of an ordered array of nanoparticles (NPs) composed of one material surrounded by a matrix composed of another material, are a popular form of 3D PhCs. The term “colloidal crystal” often refers to a close-packed array of solid NPs surrounded by air or

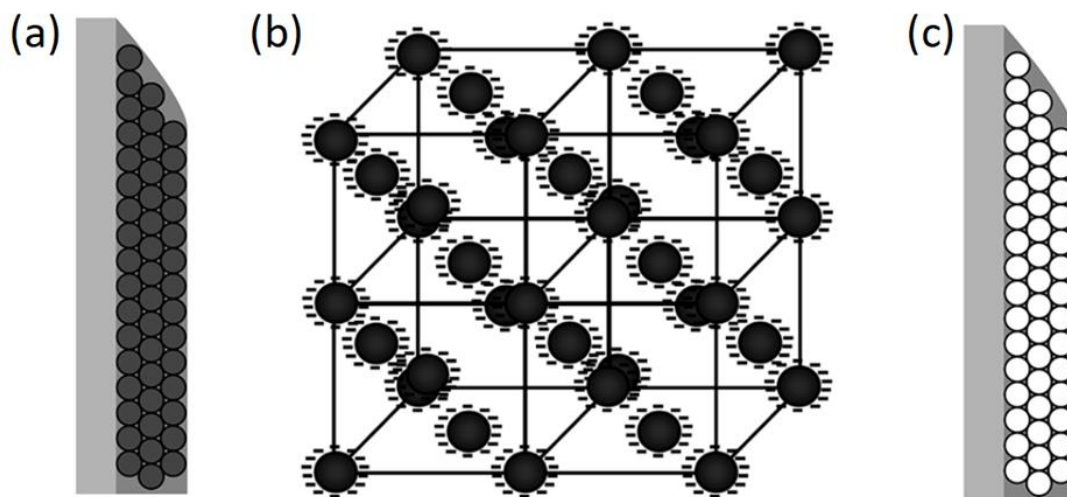


Figure 2. Graphic representations of various types of colloidal crystals. (a) A colloidal crystal consisting of a close-packed array of NPs surrounded by another material. (b) A non-close-packed CCA consisting of highly-charged NPs repelling one another in a liquid. (c) A close-packed inverse opal consisting of air voids surrounded by solid material. a & c reprinted with permission from Solid Deep Ultraviolet Diffracting Inverse Opal Photonic Crystals, K.T. Hufziger, A.B. Zrimsek, S.A. Asher, *ACS Appl. Nano Mater.* 2018, 1, 12, 7016-7024; DOI: [10.1021/acsnm.8b01806](https://doi.org/10.1021/acsnm.8b01806). Copyright 2018 American Chemical Society. b reprinted with permission from Polymerized Crystalline Colloidal Array Sensing of High Glucose Concentrations, M.M. Ward Muscatello, L.E. Stunja, S.A. Asher, *Anal. Chem.* 2009, 81, 12, 4978-4986; DOI: [10.1021/ac900006x](https://doi.org/10.1021/ac900006x). Copyright 2009 American Chemical Society.

another material. (Figure 2a) However, other types of colloidal crystals exist. Crystalline colloidal arrays (CCAs) consist of a non-close-packed array of NPs suspended in a medium. (Figure 2b) The Asher group has fabricated CCAs since the early 1980s and utilized their diffraction properties for a variety of purposes, including as wavelength rejection filters,^{6, 7} sensors,⁸⁻¹¹ and wavelength-selecting devices (WSDs) for spectrometers.^{12, 13} Another common type of colloidal crystal is the inverse opal (IO), which consists of an ordered array of air voids surrounded by a solid matrix material. (Figure 2c) IOs have been shown in the literature to be useful for a variety of applications, such as optoelectronics,^{14, 15} sensing,¹⁶⁻¹⁸ and energy storage.¹⁹⁻²¹ IOs are typically close-packed, though non-close-packed IOs have been reported.^{22, 23} IOs are most commonly fabricated by filling the interstitial space between the NPs of a colloidal crystal with another material, then removing the NPs to “invert” the PhC.

Colloidal crystals are typically fabricated by self-assembly of the NPs. A balance between van der Waals attraction, electrostatic repulsion, capillary forces, and other forces is required to achieve sufficiently well-ordered structures.²⁴ Colloidal crystals tend to self-assemble into face-centered cubic (fcc) structures, as fcc is the structure with the lowest free energy.²⁵ However, the free energy difference between fcc and other structures is relatively small ($\sim 10^{-3}kT$ per particle lower than hexagonal close-packed, for example), so stacking faults and other packing defects can occur.²⁵ It has been observed that the fcc structures generally form with their (111) planes lying parallel to the surface of the substrate onto which the structures self-assemble.²⁶ Therefore, these (111) planes serve as the diffracting basis for most applications of self-assembled fcc colloidal crystals.

Many self-assembly techniques have been described in the literature, including Langmuir-Blodgett,^{27, 28} centrifugation,^{29, 30} spin-coating,^{31, 32} and vacuum filtration.^{33, 34} However,

evaporative self-assembly techniques are most commonly used because they do not produce certain defects common to other techniques, such as differently-oriented domains.²⁶ Two main types of evaporative self-assembly exist: vertical self-assembly³⁵⁻³⁷ and inward-growing (or horizontal) self-assembly.^{26, 38, 39} In vertical self-assembly, a substrate is vertically immersed in a vial containing an evaporating suspension of NPs. In contrast, for inward-growing self-assembly, the suspension of NPs is dropped directly onto a horizontal substrate and allowed to evaporate. For both methods, a thin PhC film is deposited onto the substrate as the NPs pack at the substrate-liquid-air contact line during evaporation.

1.1.3 Deep UV Resonance Raman Spectroscopy of Explosives

As mentioned in section 1.1.2, the Asher group previously used a deep UV resonance Raman (DUVRR) spectrometer equipped with a CCA-based WSD for standoff detection of explosives.¹³ Other common explosives detection methods, such as canine olfaction, colorimetric assays, and ion mobility spectrometry, require people, animals, or instruments to be physically near (or in direct contact with) the potential explosive.^{13, 40} Therefore, the standoff capabilities of DUVRR spectroscopy are very desirable because explosives can be detected in the field without risking loss of life or damage to equipment.

Exciting explosive samples with deep UV light is ideal for standoff detection. The intensity of scattered light is proportional to ν^4 , and is therefore inversely proportional to λ^4 .^{13, 41} Therefore, UV excitation results in more intense scattering than visible or infrared excitation. Additionally, many explosive compounds absorb deep UV light.^{42, 43} (Figure 3) Exciting explosive samples within these deep UV absorption bands leads to resonance enhancement of the resulting Raman signal, greatly improving signal-to-noise (S/N).^{13, 42, 43}

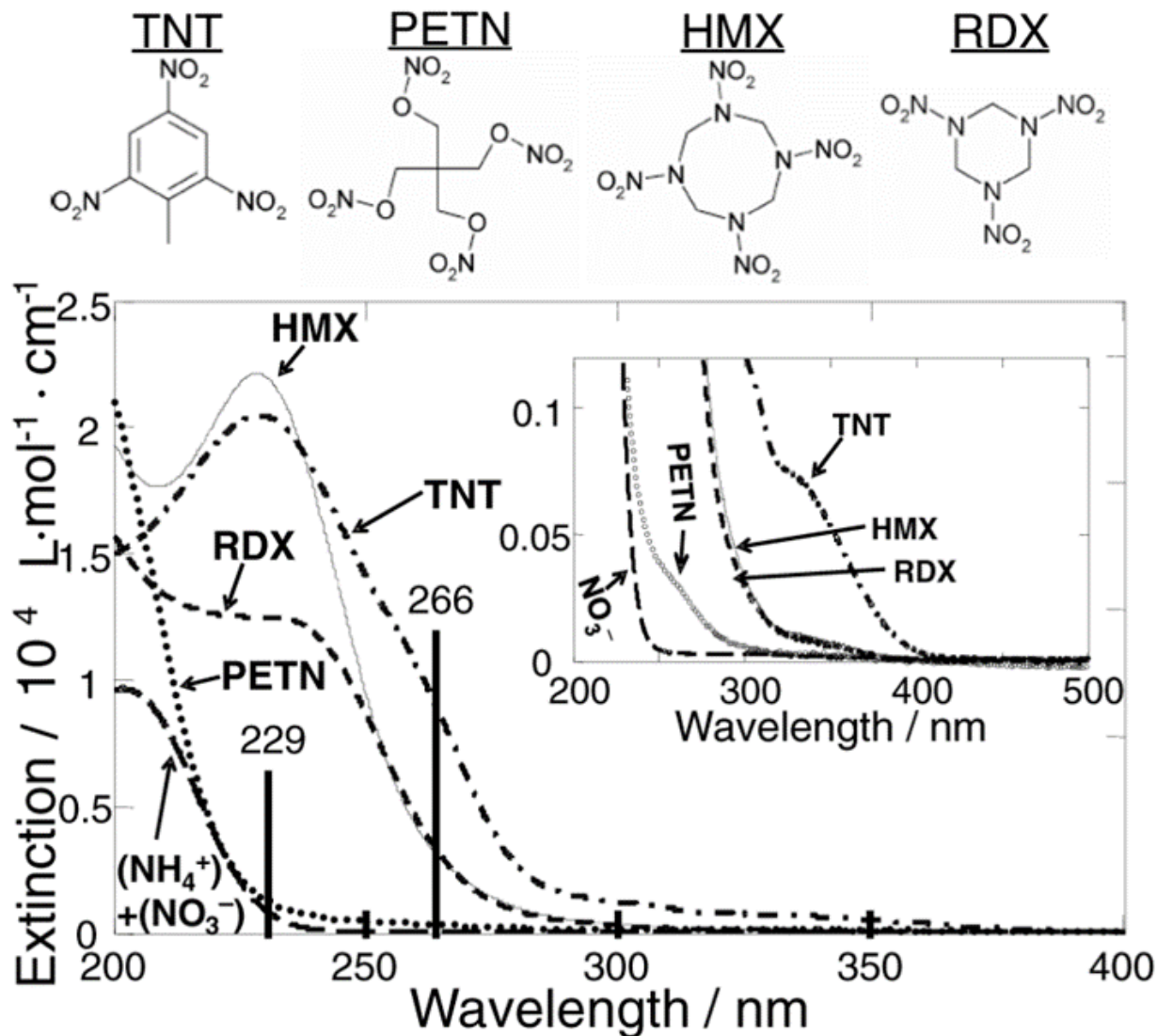


Figure 3. Chemical structures and molar absorptivities of some common explosives. Additionally, two UV laser wavelengths (229 nm and 266 nm) are marked. Excitation of these compounds at these wavelengths would yield resonance enhancement of the resulting Raman signal. Reprinted with permission from Deep UV Resonance Raman Excitation Enables Explosives Detection, D.D. Tuschel, A.V. Mikhonin, B.E. Lemoff, S. A. Asher, *Appl. Spectrosc.*, 2010, 64, 425-432; DOI: [10.1366/000370210791114194](https://doi.org/10.1366/000370210791114194). Copyright 2010 SAGE Publishing.

Wide-field Raman imaging spectrometers use a defocused laser beam to excite a large region of the sample.^{12, 44} The Raman-scattered light is collected by a telescope and focused onto a WSD to select a narrow range of wavelengths to be sent to the detector. In the ideal case, only wavelengths corresponding to Raman bands from the analyte(s) of interest are sent to the detector. Because of the need to select narrow Raman bands, the diffraction bandwidths of these WSDs should be as small as possible to ensure selectivity of the spectrometer.¹³

1.2 Prior Work

1.2.1 Development of CCA Deep UV WSDs

Due to a lack of commercial deep UV WSDs, the Asher group had to develop an optimal WSD for use in the deep UV. The first attempt at developing such a device used a CCA consisting of silica (SiO₂) NPs suspended in water.¹³ Silica was chosen as the NP material because it does not significantly absorb deep UV light, unlike other NP materials like polystyrene (PS) or poly(methyl methacrylate) (PMMA). The CCA was used as a WSD in a standoff wide-field DUVRR imaging spectrometer to image pentaerythritol tetranitrate (PETN) and ammonium nitrate (NH₄NO₃) at concentrations as low as 10 μg/cm² from a distance of 2.3 m.¹³ The CCA had a diffraction bandwidth of 1 nm, allowing for the selection of relatively narrow Raman shift ranges of <200 cm⁻¹.¹³ By changing the angle between the CCA normal and the collected Raman-scattered light, the spectrometer was able to select Raman bands corresponding to PETN and NH₄NO₃ without interference from other bands.¹³ The primary disadvantage to using the CCA as a WSD was that the CCA was not stable for long periods of time. The ordering of the silica NPs could be

easily disrupted by photochemistry, mechanical disturbance, temperature changes, and evaporation of the water.³

1.2.2 Development of IO Deep UV WSDs

To produce a more stable WSD, our group proposed that a solid PhC would alleviate the instability observed for CCAs. An adaptation of vertical self-assembly, based on the co-assembly method of Hatton et al.,⁴⁵ was used to form a close-packed array of PSNPs and simultaneously form a network of silica around the PSNPs.³ The silica network was formed by sol-gel hydrolysis (Figure 4a) and condensation (Figure 4b) of tetraethyl orthosilicate (TEOS) during the evaporative self-assembly.⁴⁶ Subsequent removal of the templating PSNPs from the silica network yielded a silica IO which Bragg diffracted deep UV light. This IO proved much less prone to degradation over time, as the stopband properties showed little change >100 days following fabrication.³

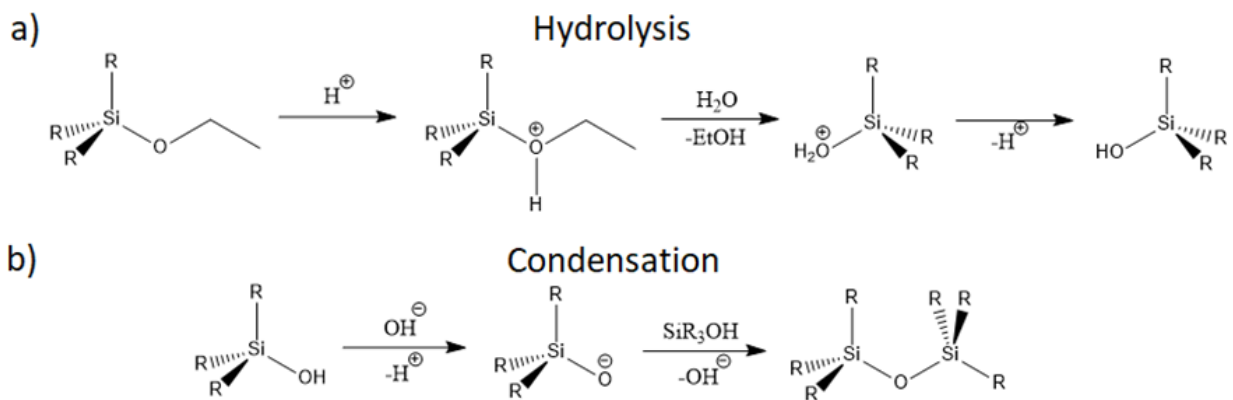


Figure 4. Hydrolysis and condensation of TEOS to form silica. (a) Acid-catalyzed hydrolysis of TEOS and its derivatives. Upon completion of hydrolysis, each ethoxy group is replaced by a hydroxyl group. (b) Condensation of TEOS derivatives to form silica. Following complete condensation, each Si atom will have siloxane (Si-O-Si) bonds to four other Si atoms. Each R group can be -OEt, -OH, or -OSi, depending on hydrolysis and/or condensation reactions that have previously occurred at those sites.

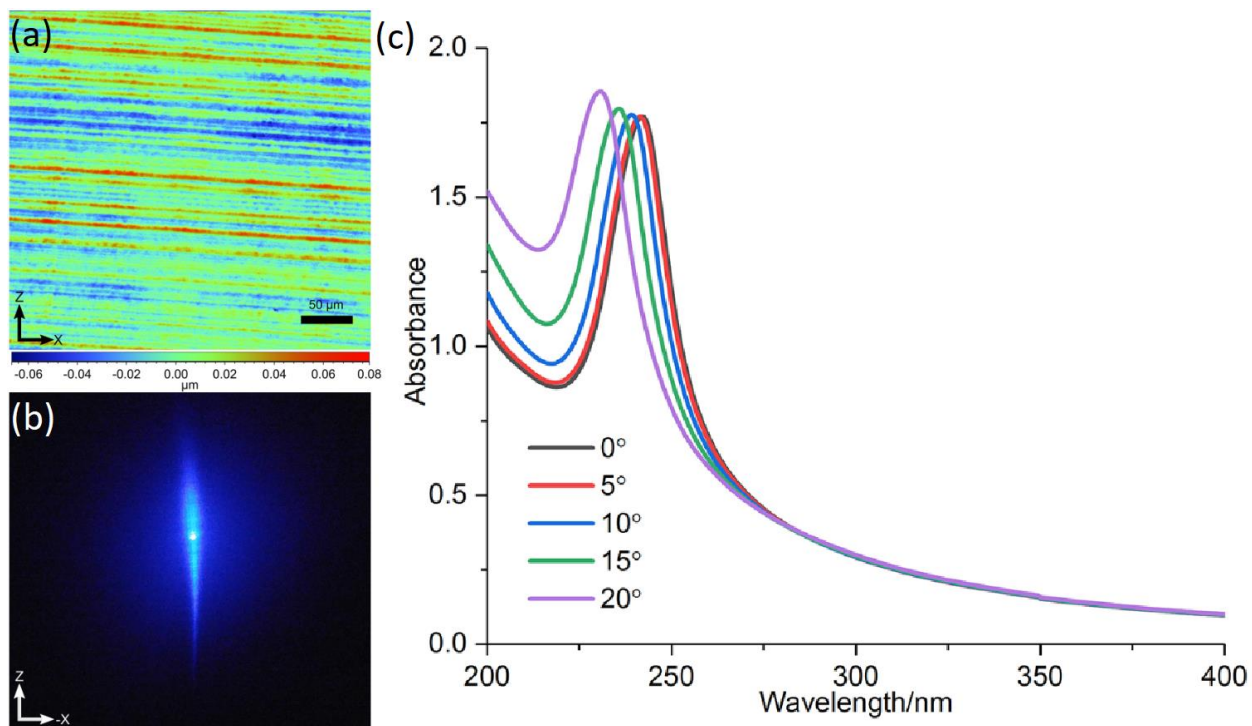


Figure 5. Characterization of inverse opals fabricated by vertical co-assembly. (a) Optical profilometry image of an inverse opal fabricated by vertical self-assembly. Here, red represents thicker sample regions, while blue represents thinner regions. (b) Shape of the 229 nm beam diffracted by the inverse opal. The beam shape is distorted to a line rather than a single spot. (c) Extinction spectra from the same inverse opal recorded at various incident angles. Notably, the baseline extinction rapidly increases as wavelength decreases. The phenomena observed in (b) and (c) can be directly attributed to diffuse scattering from the striations observed in (a). Reprinted with permission from Solid Deep Ultraviolet Diffracting Inverse Opal Photonic Crystals, K.T. Hufziger, A.B. Zrimsek, S.A. Asher, *ACS Appl. Nano Mater.* 2018, 1, 12, 7016-7024; DOI: [10.1021/acsnm.8b01806](https://doi.org/10.1021/acsnm.8b01806). Copyright 2018 American Chemical Society.

Despite the improved stability of the silica IO, this IO was not suitable for use as a deep UV WSD. The vertical self-assembly method produces PhCs which exhibit irregularly-spaced groove-like features called striations on the surface of the PhC.^{3, 47, 48} (Figure 5a) These striations result from the accumulation of PSNPs at various points on the substrate surface as the substrate-liquid-air contact line pins and depins during the self-assembly. Diffuse scattering from these striations distorted the projected shape of the diffracted laser beam into a line rather than a single spot.³ (Figure 5b) This diffuse scattering was also believed to be the cause of the increasing baseline extinction observed in the deep UV region of the extinction spectrum of the IO.³ (Figure 5c) At the stopband center wavelength, ~80% of the incident light was diffusely scattered rather than Bragg diffracted.

Additionally, the measured laser diffraction bandwidth (full width at half-maximum, FWHM) of the IO (16.8 nm) was much broader than that of the CCA (1 nm). As discussed in section 1.1.1, there are two known contributing factors for the change in diffraction bandwidth. First, the refractive index contrast between silica and air (for the IO) is much greater than that between silica and water (for the CCA). Second, close-packed structures will likely have greater variation in their periodicity compared to non-close-packed structures. Periodicity is directly proportional to NP diameter for close-packed fcc structures (Equation 3).² Since not all NPs have the exact same diameter, increased variation in periodicity leads to larger diffraction bandwidths, as a larger range of wavelengths fit various local Bragg conditions. Therefore, similar bandwidths to those of the CCAs cannot be achieved without also implementing other supplementary methods, such as narrowing the refractive index contrast.

$$D = d_{NP} \times 0.816 \quad \text{Equation 3}$$

2.0 Experimental

2.1 Horizontal Co-Assembly Procedure

2.1.1 Substrate Preparation

Prior to each co-assembly, 6 quartz microscope slides (Technical Glass Products GE-124, $25 \times 25 \times 1 \text{ mm}^3$) were immersed in 80 mL of a freshly-prepared piranha solution for 3 hr. The piranha solution was a 3:1 v/v mixture of sulfuric acid (H_2SO_4 , 98%, Fisher) and hydrogen peroxide (H_2O_2 , 30%, Fisher). Following this treatment, the slides were rinsed with nanopure water (Barnstead Infinity, $18\text{M}\Omega\cdot\text{cm}$) and immersed in ~ 100 mL of nanopure water for 1 hr. The slides were dried with a nitrogen stream prior to use.

2.1.2 Colloidal Suspension Preparation

A solution consisting of a 2:2:3 volume ratio of tetraethyl orthosilicate (TEOS, Aldrich), hydrochloric acid (HCl, Fisher, diluted to 0.1 M with nanopure water unless otherwise specified), and ethanol (Decon Labs, 200 proof) was mixed at room temperature for 3 hr (unless otherwise specified) at 500 rpm (LP Vortex Mixer, Thermo Fisher). This solution will hereafter be referred to as “TEOS solution”. After mixing, a suspension consisting of 2.3% v/v polystyrene nanoparticles (PSNPs, unless otherwise specified, full PSNP synthesis details in Appendix A) and 6% v/v TEOS solution (unless otherwise specified) was prepared with nanopure water and mixed

at room temperature for 1 hr at 500 rpm. This suspension will hereafter be referred to as “PSNP/TEOS suspension”.

2.1.3 Preparation of PS/SiO₂ Photonic Crystals

The substrates were placed on a raised platform atop a vibration isolation platform (BT-2024, Newport) inside an environmental control chamber (ECC, Darwin Chambers). 200 μ L (unless otherwise specified) of the PSNP/TEOS suspension was pipetted onto each substrate. The suspension spread to cover the entire top surface of the substrate without assistance. To prevent direct air flow onto the evaporating suspension, the substrates were covered with a plastic tub (Rubbermaid, 22 \times 20 \times 12 cm³). The environmental conditions of the chamber were set to 20°C and 75% relative humidity, which were typically achieved in <15 minutes. The relative humidity typically increased to ~90% (Fisher Traceable Hygrometer) during the evaporation, then reduced to that of the ECC. Upon overnight evaporation of the colloidal suspension, a thin film consisting of a close-packed array of PSNPs surrounded by a network of silica formed.

2.2 Inverse Opal Fabrication

PS/SiO₂ PhCs fabricated by horizontal co-assembly were heated to 70°C (Thermo Scientific Heratherm OMH60) for at least 2 days to induce condensation of the silica network. Following heating, each PhC was placed in a 30 mL beaker with ~20 mL of tetrahydrofuran (THF) for 3 hr to dissolve most of the PSNPs. After being allowed to dry, each PhC was placed in another 30 mL beaker with ~20 mL of piranha solution for 3 hr to remove the remaining PSNPs. The PhCs

were then placed in another 30 mL beaker with ~20 mL of water for 30 minutes, then dried with a nitrogen stream.

2.3 Characterization of Stopband Properties

Diffraction properties of the PhCs were evaluated using a UV-vis absorption spectrometer (Agilent Cary 5000) in single beam mode with a 2 nm spectral resolution, a 100 ms averaging time, and a 600 nm/min scan rate. PhC samples were mounted on a microscope slide holder (Thorlabs XYFM1) equipped with translational stages to move different regions of the sample into the path of the beam. This microscope slide holder was mounted onto a rotational stage (Newport 481-A) to be able to vary the angle of the incident light beam relative to the PhC normal.

2.4 Measurement of Structural Dimensions

The air void dimensions of IO samples were measured by scanning electron microscopy (SEM). The IOs were broken in half and mounted onto vertical SEM mounts to image the internal structures from the side. Samples were gold coated for 75 s at 30 mA prior to imaging. 15 measurements of each relevant dimension were recorded using ImageJ (NIH) and averaged.

2.5 Filling Inverse Opal Voids with Water

The IO sample was placed inside a 40 mm quartz fluorimeter cell (Starna Cells 3-Q-40) with the substrate side of the sample placed against the back wall of the cell. The cell was mounted on the microscope slide holder detailed in section 2.3. The cell was filled with nanopure water until the water level was above the top of the IO. Extinction spectra were recorded using the same settings described in section 2.3. The cell and sample were dried with a stream of nitrogen and extinction spectra were recorded again.

3.0 Development of Inward-Growing Co-Assembly of Polystyrene/Silica Photonic Crystals

3.1 Motivation

As mentioned in section 1.2, previous attempts by the Asher group to fabricate PhC-based deep UV-diffracting WSDs did not provide WSDs that were suitable for use in spectrometers. Aqueous CCAs allowed for the selection of relatively narrow Raman shift ranges ($<200\text{ cm}^{-1}$), but their long-range order could not be maintained for long periods of time.³ Solid IOs fabricated by vertical co-assembly were plagued by large diffraction bandwidths (16.8 nm) and diffuse scattering of the majority of the incident light, caused by striations on the IO surface.³ It was clear that a different approach would be necessary to fabricate a WSD which was indefinitely stable but also had relatively low diffuse scattering in the deep UV region.

To achieve this goal, we proposed adapting the inward-growing self-assembly method^{26, 38, 39} to co-assemble PSNPs with TEOS. An aqueous suspension of PSNPs would be combined with a solution of hydrolyzed TEOS and deposited onto a hydrophilic quartz substrate. Upon evaporation of the liquid, the PSNPs would form a close-packed fcc structure, while the hydrolyzed TEOS would undergo condensation reactions to form a network of silica around the PSNPs. Inward-growing self-assembly has been shown to produce PhCs that lack striations in the thin film covering most of the substrate surface.⁴⁹ Therefore, we believed that upon removing the PSNPs, IOs fabricated by this inward-growing co-assembly method would be stable long-term and diffract deep UV light with low diffuse scattering.

3.2 Mechanism of Inward-Growing Co-Assembly

Inward-growing self-assembly uses the evaporation of an aqueous suspension of PSNPs to deposit an ordered thin film of PSNPs onto a substrate. At the beginning of the evaporation, the edges of the evaporating drop are pinned to the edges of the substrate. In this regime, the evaporation rate at the edges of the drop is greater than that at the center.⁴⁹ Therefore, there exists a flow of PSNPs from the center of the drop toward the edges, in accordance with the coffee ring effect.^{26, 49, 50} The flow of PSNPs toward the edges of the drop results in a buildup of PSNPs at the substrate edges known as the “coffee ring”, due to the analogous behavior of drying drops of coffee. After substantial evaporation, the edges of the drop depin from the edges of substrate and move inward toward the center of the substrate. As the evaporation front moves across the substrate, a thin PSNP film of nearly constant thickness is deposited. (Figure 6) Though this film region contains substantially fewer layers of PSNPs than the coffee ring at the edges, the PSNPs are typically better ordered and therefore give rise to more intense and narrower photonic stopbands. Crucially, comparing Figure 6 to Figure 5a, it is apparent that the inward-growing co-assembly method does not result in the striations observed for vertical co-assembly. Toward the end of the evaporation, we observe the formation of an opaque region surrounding a circular ($d \sim 1$ mm) void. The void arises from the continued flow of PSNPs to the edges of the drop until the very end of the evaporation, leaving a small region with no or very few PSNPs.

As the PSNPs self-assemble, a network of silica is formed around the PSNPs via sol-gel reactions of TEOS. Before the co-assembly, TEOS is hydrolyzed by water, a process which is catalyzed by hydrochloric acid (HCl).⁴⁶ (Figure 4a) Ethanol is used in this process as a mutual solvent of TEOS and water, which are not miscible with each other.⁵¹ Hydrolysis of TEOS results in the ethoxy groups of TEOS being replaced by hydroxyl (silanol) groups. Following hydrolysis,

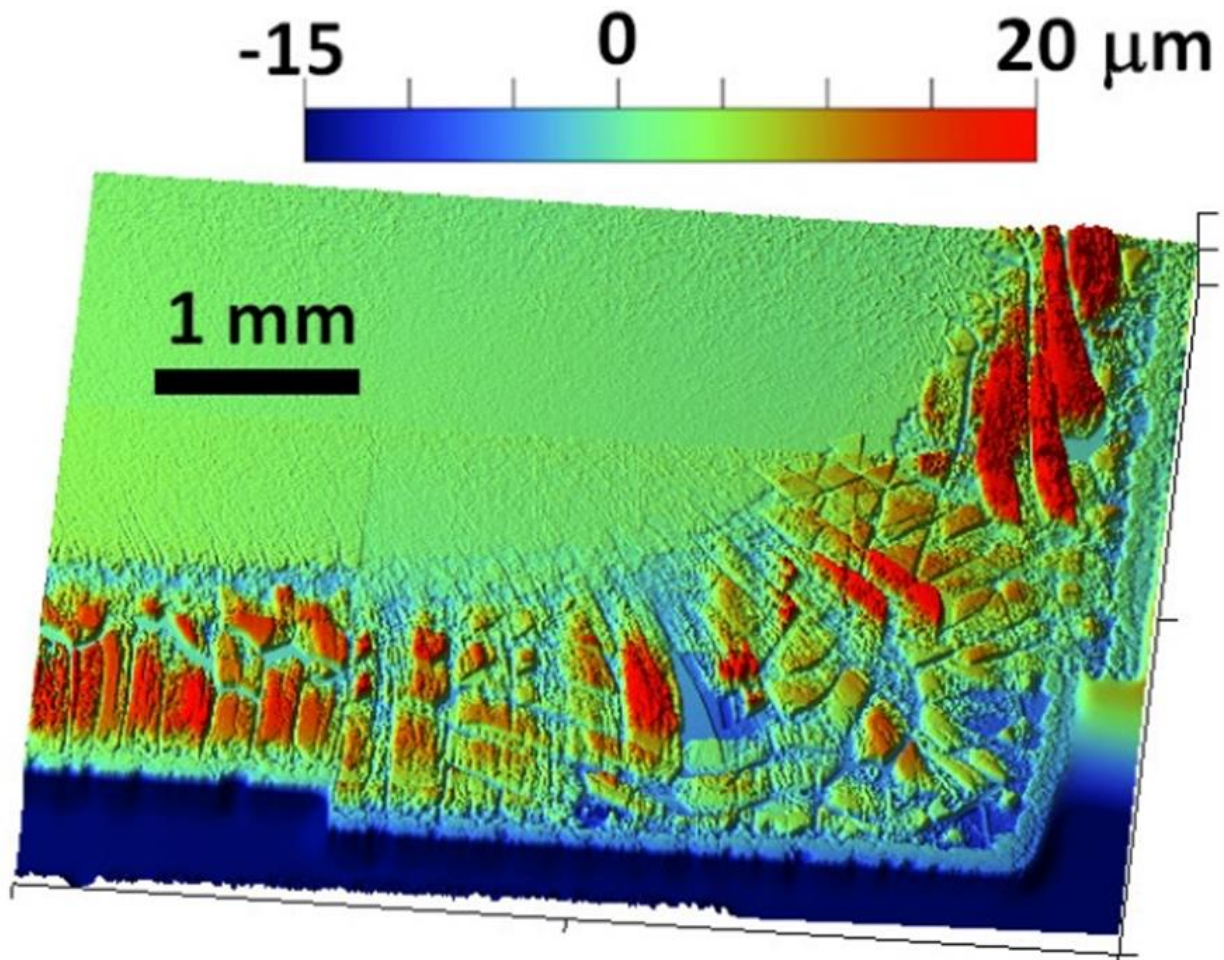


Figure 6. Optical profilometry image of the corner of a PS/SiO₂ PhC fabricated by inward-growing co-assembly of PSNPs and TEOS. The red region is the outer coffee ring, the large green region represents the ordered thin film, and the blue region indicates the substrate. It is clear that the ordered thin film lacks the periodic thickness variation observed for vertically co-assembled structures.

these hydrolyzed species attack other silicon atoms, resulting in condensation and the formation of siloxane (Si-O-Si) bonds.⁴⁶ (Figure 4b) These processes proceed until, ideally, all ethoxy groups of TEOS have been hydrolyzed, and all resulting hydroxyl groups have been condensed to form a robust network of silica around the PSNPs. Removing the PSNPs from this PS/SiO₂ PhC results in a silica IO which diffracts deep UV light.

3.3 Optimization of Fabrication Conditions

To prepare substrates for horizontal co-assembly, quartz microscope slides were immersed in piranha solution (a 3:1 v/v mixture of 98% sulfuric acid and 30% hydrogen peroxide) for 3 hr prior to use. This piranha treatment decomposes any organic contaminants on the substrate surfaces, as well as rendering the surfaces hydrophilic via oxidation.^{3, 50, 52} The substrates were then immersed in water for 1 hr to dilute and remove the piranha solution, then dried with a nitrogen stream.

To self-assemble our PS/SiO₂ PhCs, we used PSNPs fabricated in our lab by emulsion polymerization.^{13, 50, 53} The surfaces of the PSNPs were functionalized with sulfonate groups as part of the polymerization procedure. These sulfonate groups rendered the surfaces of the PSNPs highly negatively charged, allowing the PSNPs to repel each other in water and remain dispersed.⁵³ From the average of 100 PSNPs measured from transmission electron microscope (TEM) images, the average diameter of the PSNPs was determined to be 143 ± 4 nm.

3.3.1 Optimization of Environmental Conditions

Prior reports of inward-growing self-assembly have claimed fabrication of well-ordered colloidal crystals under uncontrolled ambient temperature and humidity conditions.²⁶ However, we sought to control these conditions to better optimize our fabrication method. To this end, we used an environmental control chamber (ECC) to control the temperature and humidity of the environment surrounding the evaporating PSNP/TEOS suspension. We found that setting the ECC conditions to 20°C and 75% humidity was most optimal for fabricating well-ordered PS/SiO₂ PhCs. However, we found that using the ECC resulted in significant air flow from the fans used for temperature and humidity control, greatly influencing the evaporation rate of the liquid. To solve this issue, samples were fabricated on a plastic platform under a plastic tub inside the ECC. As evaporation proceeded, the humidity inside the tub slowly rose to ~90%, then reduced to that of the ECC following the evaporation.

3.3.2 Optimization of PSNP Volume Fraction

The volume fraction of PSNPs in the suspension deposited onto the substrate required optimization to fabricate well-ordered PhCs. A too high PSNP volume fraction could lead to increased heterogeneity in the resulting PhC, due to increased opportunity for packing defects. To determine the optimal volume fraction of PSNPs in the initial suspension, PS/SiO₂ PhCs were fabricated with PSNP concentrations ranging from 1.15-3.5% v/v. The initial drop volume was kept constant at 200 μ L, the volume which consistently gave well-ordered PhCs under optimized environmental conditions and did not spill over the edges of the substrate. The volume ratio between TEOS solution and PSNPs was kept constant at 2.6 μ L of TEOS solution per 1 μ L of

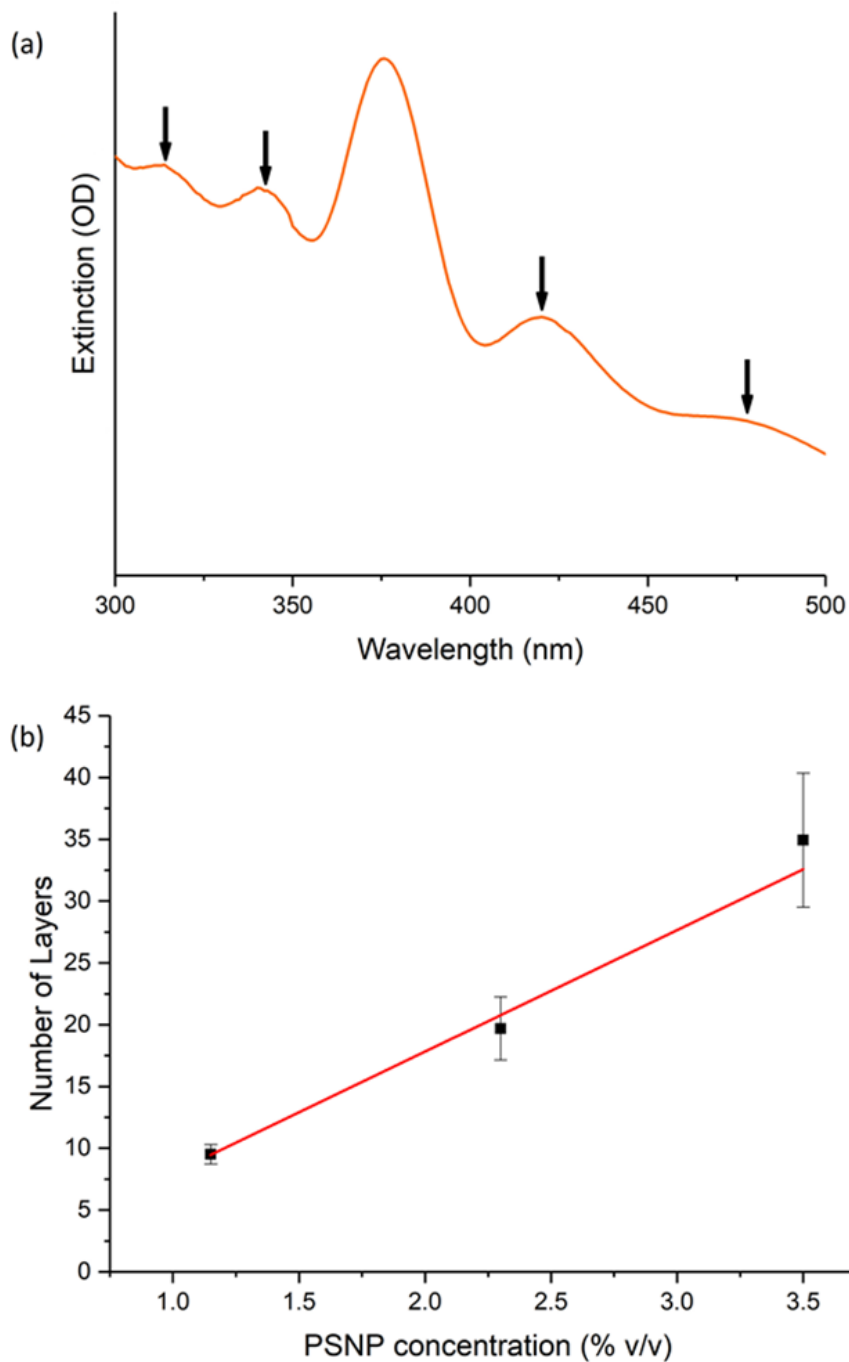


Figure 7. Determination of the optimal PSNP volume fraction. (a) Example of an extinction spectrum of a PS/SiO₂ PhC, showing Fabry-Pérot oscillations to the left and right of the stopband, indicated by arrows. (b) Number of ordered layers in PhCs resulting from inward-growing co-assembly of PS/TEOS suspensions containing various volume fractions of PSNPs. As expected, the number of ordered layers formed linearly correlated to the original PSNP concentration, but the standard deviations increase with increasing volume fraction.

PSNPs. The number of layers in each PhC was calculated from the spacing of the Fabry-Pérot oscillations (Figure 7a) in their respective extinction spectra, based on the method of Bohn et al.⁵⁴ Within this range of volume fractions, the number of ordered layers formed in the resulting PS/SiO₂ PhCs followed a roughly linear trend. (Figure 7b) However, given the large standard deviation and lack of reproducibility for 3.5% v/v PSNPs, 2.3% v/v was determined to be the optimal concentration of PSNPs for our inward-growing co-assembly method.

3.3.3 Optimization of TEOS Solution Volume Fraction

The volume fraction of TEOS solution in the PSNP/TEOS suspension also required optimization. The TEOS solution is a 2:2:3 v/v ratio of TEOS, 0.1 M HCl, and ethanol. The TEOS solution is mixed at room temperature for 3 hr to hydrolyze the TEOS prior to adding it to the PSNP suspension. Too much TEOS solution would result in the formation of layers of silica above the ordered array of PSNPs, but too little would form a fragile or discontinuous silica network between the PSNPs. At the optimal TEOS volume fraction, the interstices between the PSNPs should be completely filled with no additional silica present. To determine the optimal volume fraction of TEOS solution, PS/SiO₂ PhCs were fabricated with concentrations of TEOS solution varying from 4.5 to 16.3% v/v. The volume fraction of PSNPs was kept constant at 2.3% v/v and drop volume was kept constant at 200 μ L. At volume fractions greater than 6% v/v TEOS solution, the structures lacked defined coffee rings and were increasingly opaque due to diffuse scattering, which indicates disorder. (Figure 8) From this experiment, it was determined that the optimal volume fraction of TEOS solution for inward-growing co-assembly was 6% v/v.

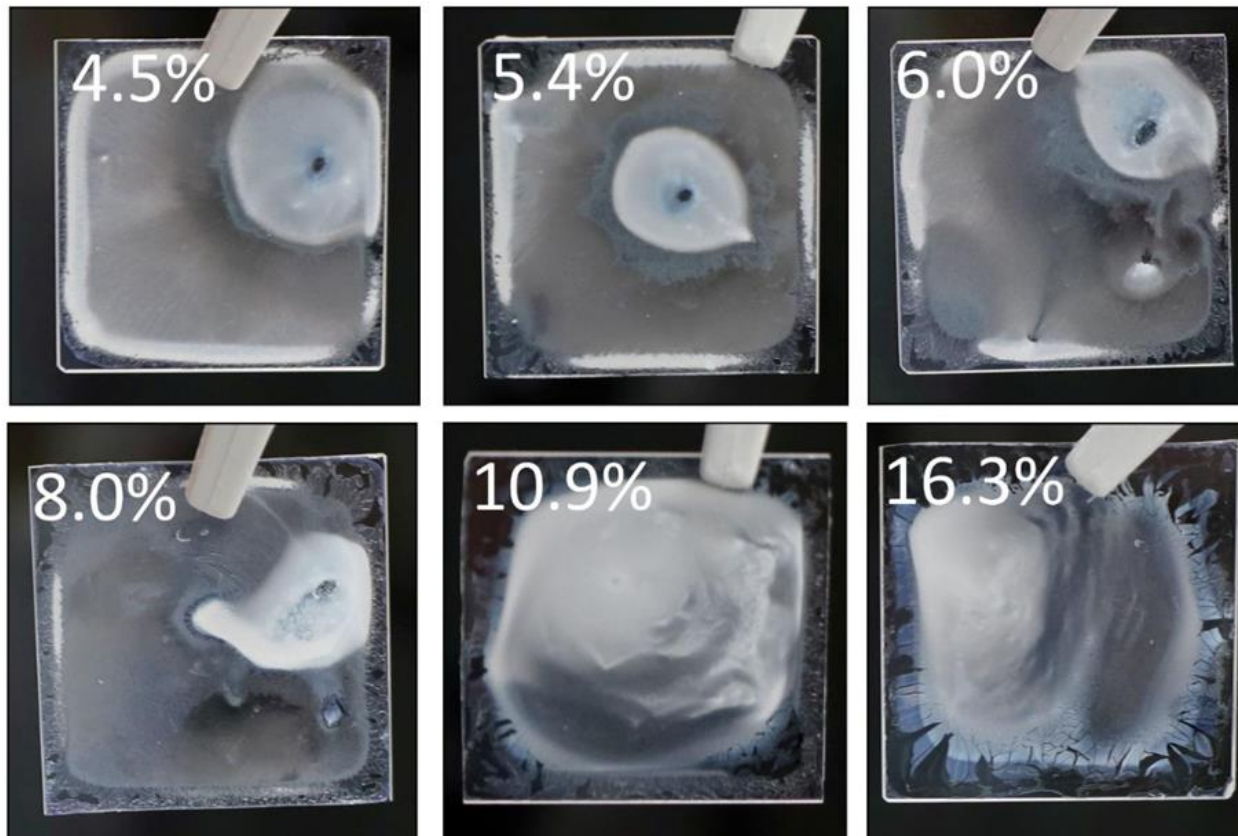


Figure 8. PS/SiO₂ PhCs fabricated with varying volume fractions of TEOS solution in the initial suspension. Starting at 8% v/v, it is apparent that the coffee ring disappears, and the films become more opaque due to diffuse scattering, indicating disorder.

3.3.4 Optimization of HCl Concentration

The concentration of HCl in the TEOS solution also required optimization. The HCl was necessary to catalyze the hydrolysis of TEOS, but an effort was made to minimize the HCl concentration to minimize pH-dependent effects on the self-assembly of PSNPs. It has previously been shown that, for inward-growing self-assembly, the best ordering is achieved when the NPs and substrate possess the same sign of surface charge.³⁸ In the case of our self-assembly of

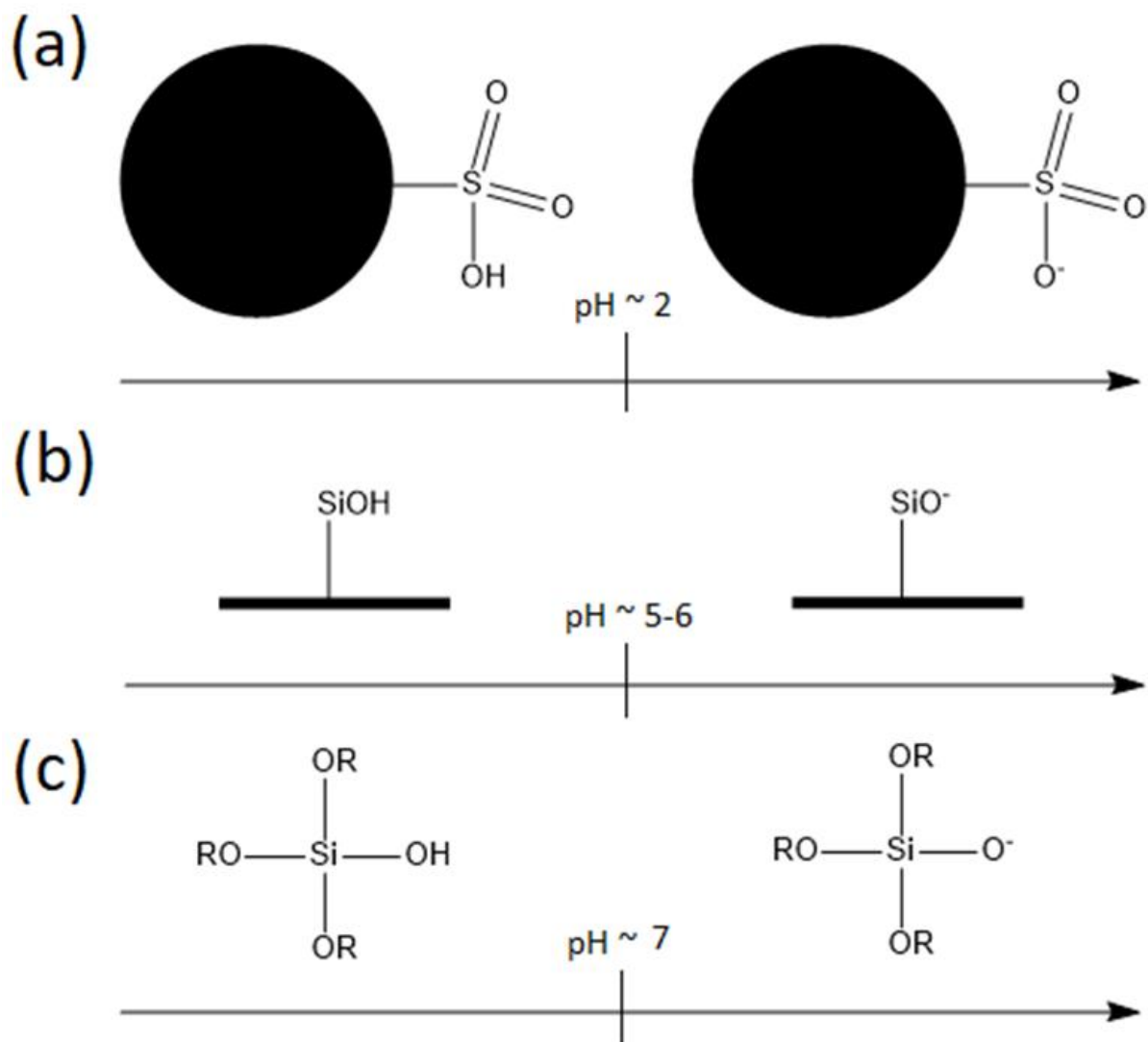


Figure 9. Dominant protonation states of species relevant to co-assembly as a function of pH. (a) Sulfonate groups on the surfaces of the PSNPs (b) Silanol groups of the quartz substrate (c) Silanol groups of hydrolyzed TEOS. The numbers stated represent the pK_a for each species. Depending on the hydrolysis and condensation reactions that previously occurred at those sites, each R group can be -Et, -H, or -Si.

negatively charged PSNPs, the best ordering should be achieved when the substrate is negatively charged as well. The high level of ordering is achieved because the particles can freely flow toward the edge of the evaporating drop without being attracted to the substrate prior to reaching the edge. The pH of the evaporating suspension affects the charges of three relevant species during self-assembly. The pK_a of the sulfonate groups on the surfaces of the PSNPs is ~ 2 .⁵⁵ Therefore, at $pH > 2$, the majority of the sulfonate groups are negatively charged, allowing for electrostatic repulsion between PSNPs. (Figure 9a) As stated previously, the quartz substrate has many surface -OH (silanol) groups from oxidation by piranha solution, which have a pK_a of $\sim 5-6$.⁵⁶ (Figure 9b) The pK_a values of the silanol groups of the various TEOS derivatives formed during hydrolysis and condensation are not as well understood. Nonetheless, a pK_a of ~ 7 for these species is generally considered a reasonable estimate.⁵⁷ (Figure 9c)

Based on these pK_a values, we believed that it would be desirable for the pH of the PSNP/TEOS suspension to be as high as possible. By allowing all the relevant species to be as negatively charged as possible, we believed that the best possible ordering of the PSNPs could be achieved. To test this hypothesis, PS/SiO₂ PhCs were fabricated using 0.1 M and 0.001 M HCl in the TEOS solution. Assuming that the pH of the PSNP/TEOS suspension is primarily determined by the volume and concentration of HCl added, these concentrations result in pH values of 2.8 and 4.8, respectively. Testing with pH paper confirmed the pH values to be ~ 3 and ~ 5 . Both HCl concentrations gave rise to well-ordered structures showing photonic stopbands. Samples fabricated with 0.001 M HCl had their normal-incidence stopbands at 360 nm, indicating close-packed fcc PSNPs with little silica in the interstices between the PSNPs. In contrast, 0.1 M HCl yielded less intense normal-incidence stopbands at 375 nm. The decrease in stopband intensity and increase in stopband wavelength indicate increased refractive index of the interstices between the

PSNPs. Therefore, with a higher acid concentration, more space in the interstices is filled by silica rather than air. To compare the silica networks formed with each HCl concentration, the samples were imaged by scanning electron microscopy (SEM). In order to more clearly image the silica networks, the PSNPs were removed by dissolving them in tetrahydrofuran (THF) for 3 hr prior to imaging. The micrographs showed that, when 0.1 M HCl is used, a silica network with long-range order and few point defects is formed (Figure 10a & c). In contrast, such a network is not formed when 0.001 M HCl is used. (Figure 10b & d) Therefore, the finding by other authors that 0.1 M HCl is optimal for vertical co-assembly procedures also holds for our inward-growing co-assembly method.^{3, 45}

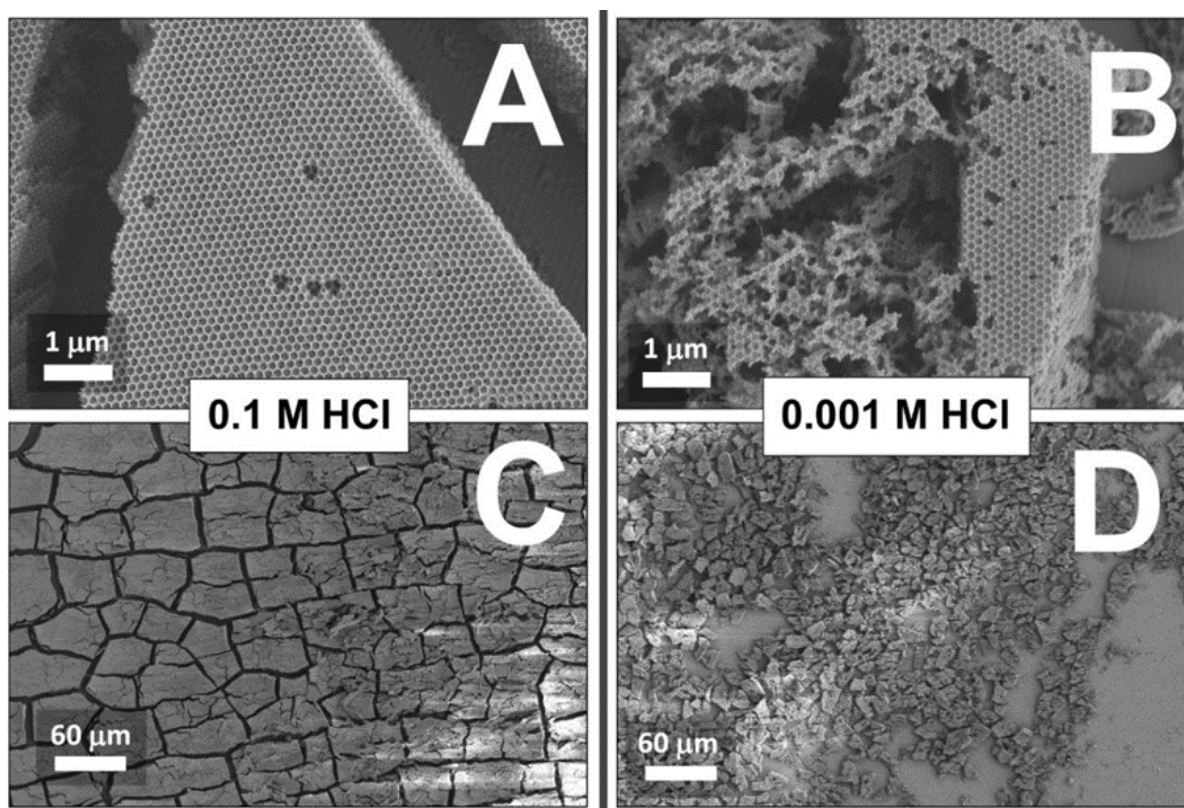


Figure 10. Effect of pH on the formation of robust silica networks. The PSNPs were removed prior to recording SEM images in order to clearly image the silica networks. Silica networks fabricated with 0.1 M HCl in the TEOS solution (a & c) are much more robust with more long-range order than those fabricated with 0.001 M HCl (b & d).

4.0 Fabrication of Deep UV-Diffracting Silica Inverse Opals

4.1 Removal of PSNPs from PS/SiO₂ Photonic Crystals

In order to fabricate deep UV-diffracting WSDs, it was necessary to remove the PSNPs from the PS/SiO₂ PhCs. The reasoning for removing the PSNPs was two-fold. First, at the PSNP diameter used (143 ± 4 nm), the PS/SiO₂ PhC Bragg diffracted at 375 nm at normal incidence. Therefore, removing the PSNPs to lower the effective refractive index of the PhC was necessary to fabricate a deep UV-diffracting structure. Second, and more importantly, PS significantly absorbs deep UV light, while silica does not.¹³ Therefore, silica is an ideal material for deep UV-diffracting devices, while the presence of PSNPs would inhibit deep UV diffraction.

There exist two types of methods for removal of polymer NPs from a silica matrix to form IOs. Solvent-based methods involve immersing the polymer/SiO₂ PhC in a solvent known to either dissolve or decompose the polymer NPs, such as toluene,⁵⁸ THF,⁵⁸ and/or piranha solution.³ Calcination-based methods involve heating the PhC to very high temperatures ($\geq 500^\circ\text{C}$) to combust the polymer NPs.^{45, 58} Calcination is known to have the added benefit of inducing condensation reactions which form covalent bonds between the silica network and the substrate, as well as within the network itself.⁵⁸ (Figure 4b) These condensation reactions render the silica network more mechanically robust. However, as a result of these condensation reactions, calcination causes compression of the network along the substrate normal. Solvent-based methods, meanwhile, result in significantly less compression, as fewer condensation reactions result from this type of removal.⁵⁸ Therefore, we desired to optimize a solvent-based PSNP removal method to limit the compression of the silica network.

Our first attempt at a solvent-based removal consisted of immersing the PS/SiO₂ PhC in ~30 mL of THF for 3 hr. THF was chosen because PS is known to be soluble in THF (solubility = 0.96 g/mL at 25°C).⁵⁹ However, in accordance with prior reports by our group for vertical co-assembly,³ this THF treatment was insufficient for the fabrication of deep UV WSDs, as the resulting structures still absorbed deep UV light. The absorption likely results from two sources. First, it is possible that the THF did not fully remove the PSNPs from the PS/SiO₂ PhC, and that some residual PS was left behind. Second, any residue of THF remaining after treatment would also absorb deep UV light, as the UV cutoff for THF (defined as the wavelength at which a 1 cm path length absorbs >90% of incident light) is 215 nm.⁶⁰

To eliminate this deep UV absorption, the samples were immersed in piranha solution for 3 hr following the THF treatment. The samples were kept in water for 30 min afterward to dilute and remove the piranha solution, then dried with a stream of nitrogen. This solvent treatment yielded deep UV-diffracting IOs with normal-incidence stopbands ranging from ~220-235 nm. The lack of deep UV absorption in the extinction spectra of these IOs confirmed that piranha solution decomposed all THF and PS.

4.2 Robustness of the Silica Network

4.2.1 Robustness at the Time of PSNP Removal

During initial solvent-based PSNP removals, it was often observed that some portions of the silica network delaminated from the substrate. It was believed that the network delaminated because insufficient siloxane (Si-O-Si) bonds had formed between the network and the substrate,

or within the network itself. As mentioned in section 4.1, heating is known to promote condensation reactions, (Figure 4b) which would strongly adhere the silica network to the substrate by forming covalent bonds. Therefore, we decided to heat PS/SiO₂ PhCs to 70°C for 2 days before attempting solvent-based removal of the PSNPs. 70°C was chosen as the optimal temperature because it is significantly below the glass transition temperature of PS (~100°C),⁶¹ leaving the PSNPs intact as a template for the silica network. Additionally, these conditions roughly mimic the conditions used for vertical co-assembly methods (2-4 days at 50-70°C), during which a robust silica network is formed.^{3,45,58} Following this heating, the silica network remained adhered to the substrate following 3 hr immersions in THF and piranha solution, demonstrating that the silica network was now more robust.

To compare the diffraction of IOs fabricated by this solvent-based treatment and calcination, extinction spectra of an IO were recorded after solvent treatment and after calcination. The normal-incidence stopband of the solvent-treated IO was centered at 235 nm. However, the Bragg-Snell Law (Equation 1), predicts $\lambda = 269 \pm 7$ nm, taking $D = 0.816 \times (143 \pm 4$ nm) = 117 ± 3 nm,² $f_{silica} = 0.26$, $f_{air} = 0.74$, $n_{silica, 269} = 1.5028$,⁶² and $n_{air} = 1.00$. Therefore, it was believed that solvent treatment had not fully prevented compression of the IO along the normal. Notably, the normal-incidence stopband occurred at a higher wavelength than after calcination, as the stopband was centered at 214 nm following calcination. (Figure 11) This finding reflects prior results showing that calcination induced greater compression of the silica network than solvent-based removal.⁵⁸ This experiment showed that while heating at 70°C was sufficient to prevent delamination of the silica network, it did not fully prevent compression of the silica network upon PSNP removal.

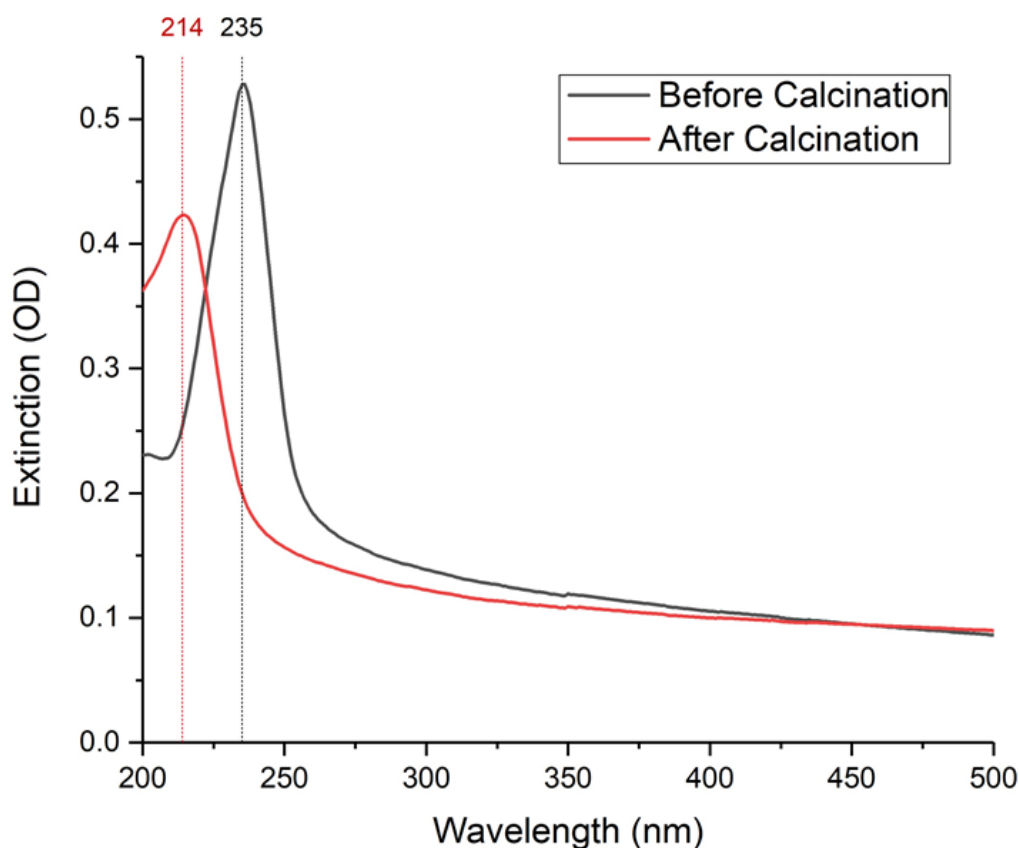


Figure 11. Comparison of extinction spectra of an inverse opal fabricated by THF/piranha treatment before and after calcination at 500°C. Following calcination, the normal-incidence stopband blue shifts by 21 nm.

To verify that the observed stopband differences were caused by compression of the silica network upon calcination, the IO samples were inspected by SEM. The IOs were broken in half in order to view the structure of the thin film that covers most of the substrate surface. Both calcination at 500°C and THF/piranha treatment resulted in some compression of the silica network perpendicular to the substrate. (Figure 12) The void height (dimension perpendicular to the substrate) for both methods was substantially smaller than the original PSNP diameter (143 ± 4 nm). (Table 1)

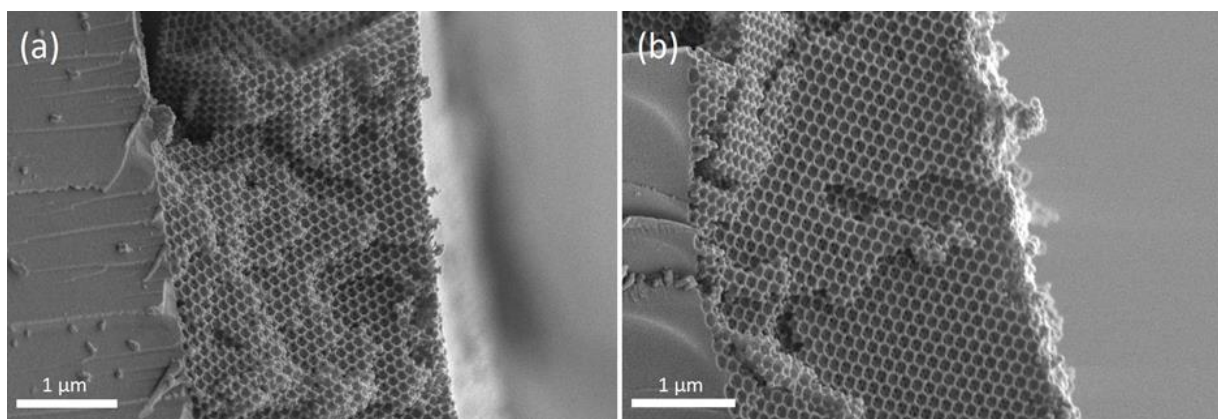


Figure 12. Side-profile SEM images of silica IOs fabricated by (a) calcination at 500°C and (b) THF/piranha solvent-based treatment.

Table 1. Effect of IO fabrication method on compression of the silica network. Noticeable differences are observed for different PSNP removal methods, with calcination resulting in more compression of the air voids perpendicular to the substrate. Additionally, the spheres compressed parallel to the substrate in regions closer to the top surface, while this effect was largely absent near the substrate.

Method	Region	Void Width (w, nm)	Void Height (h, nm)	w/h
Calcination	Surface	116 ± 4	119 ± 4	0.97 ± 0.04
	Substrate	140 ± 4	118 ± 6	1.19 ± 0.07
THF/piranha	Surface	137 ± 4	133 ± 5	1.03 ± 0.05
	Substrate	144 ± 6	123 ± 5	1.17 ± 0.06

Interestingly, notable differences were observed between the regions near the substrate and near the top IO surface. Near the substrate, the silica network could not contract parallel to the substrate, as the network was strongly adhered to the substrate. Therefore, the void widths (dimension parallel to the substrate) for both samples near the substrate are not significantly different than the original PSNP diameter. (143 ± 4 nm) The compression perpendicular to the substrate in this region was similar for both PSNP removal methods, resulting in void width-to-height (w/h) ratios that were not significantly different (~ 1.2). Nearer to the top IO surface, the silica network shrinks significantly parallel to the substrate. Due to the presence of cracks, the effects of adhesion to the substrate are much less prevalent in this region. The resulting air voids are much more spherical, as similar shrinkage occurs parallel and perpendicular to the substrate. Both calcination and THF/piranha treatments resulted in w/h ratios that were not significantly different than 1, the w/h value for a perfect sphere. The major difference between PSNP removal methods is also observed near the top surface. Calcination resulted in void dimensions of 116 ± 4 nm (width) and 119 ± 4 nm (height), while THF/piranha treatment resulted in dimensions of 137 ± 4 nm and 133 ± 5 nm. These measurements confirmed that the blue shift in the stopband upon calcination was caused by compression of the silica network, strongly supported by prior findings for vertically co-assembled IOs.⁵⁸

4.2.2 Robustness Following Removal

Based on prior findings for vertical co-assembly,³ it was initially assumed that IOs formed by inward-growing co-assembly would be indefinitely stable. However, upon recording another extinction spectrum of an IO sample 4 weeks following fabrication, it was discovered that the normal-incidence stopband had blue shifted by 12 nm. (Figure 13) Six other samples showed

smaller blue shifts (typically 3-7 nm) 17 days after PSNP removal, confirming the reproducibility of this phenomenon. Further compression of the silica network is the most likely cause of such a change, as reasonable changes in the other variables in the Bragg-Snell Law (Equation 1) would not produce a change of this magnitude. The shrinkage is believed to result from condensation reactions within the silica network following removal of the PSNPs. There are multiple possible reasons for continued condensation reactions to occur after PSNP removal. These reasons include

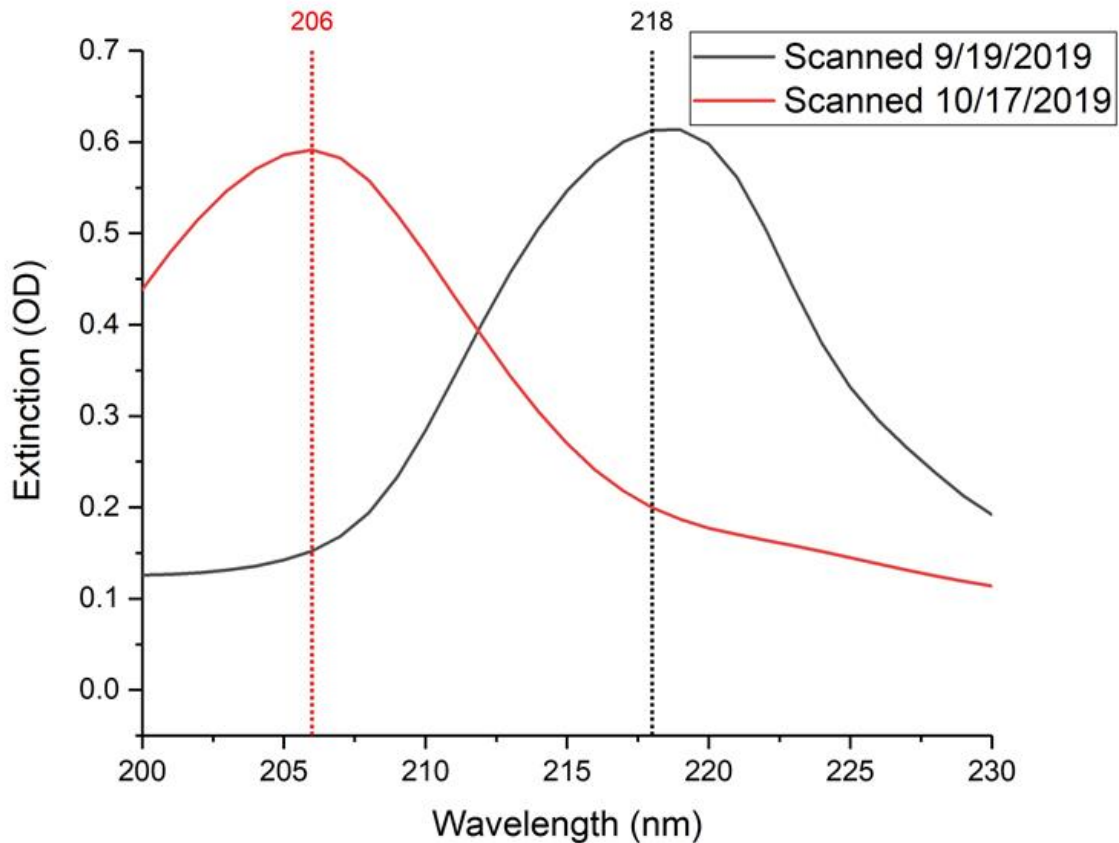


Figure 13. Comparison of extinction spectra from the same region of the same IO sample recorded immediately upon PSNP removal (black) and 28 days following PSNP removal (red). The ~12 nm blue shift over time indicates a decrease in d_{111} .

oxidation of the silica by piranha solution,⁵² depolymerization of condensed structures by excess water during co-assembly⁴⁶ or from humidity in the ambient air,⁶³ and insufficient heating to form a robust silica network.

To produce a silica network that did not shrink as much over time, we hypothesized that heating the TEOS solution prior to fabricating the PhCs would induce condensation reactions. Therefore, the resulting silica networks would contain fewer uncondensed silanol groups, reducing the amount of condensation reactions that would be possible after PSNP removal. To test this hypothesis, PhC samples were fabricated using TEOS solution that was heated to 70°C for either 0, 3, or 6 hr prior to fabricating the PhCs. Following the PhC fabrication, the samples were then heated to 70°C for 2 days and the PSNPs were removed as previously described. Over a span of three weeks, IOs fabricated with TEOS solution that was not heated at all showed an average blue shift of 7 nm. (Figure 14) Meanwhile, heating the TEOS solution to 70°C for 3 hr prior to fabricating the PhCs resulted in an average blue shift of 3 nm, and heating for 6 hr resulted in a 2 nm average blue shift. The standard deviations between the measurements for each sample also decreased as heating time increased. The decrease in standard deviation suggests that the shrinkage that did occur was more uniform across the samples fabricated with heated TEOS. This is a very promising result that indicates that the shrinkage observed for our IOs can be mitigated, if not prevented completely, with procedural optimizations.

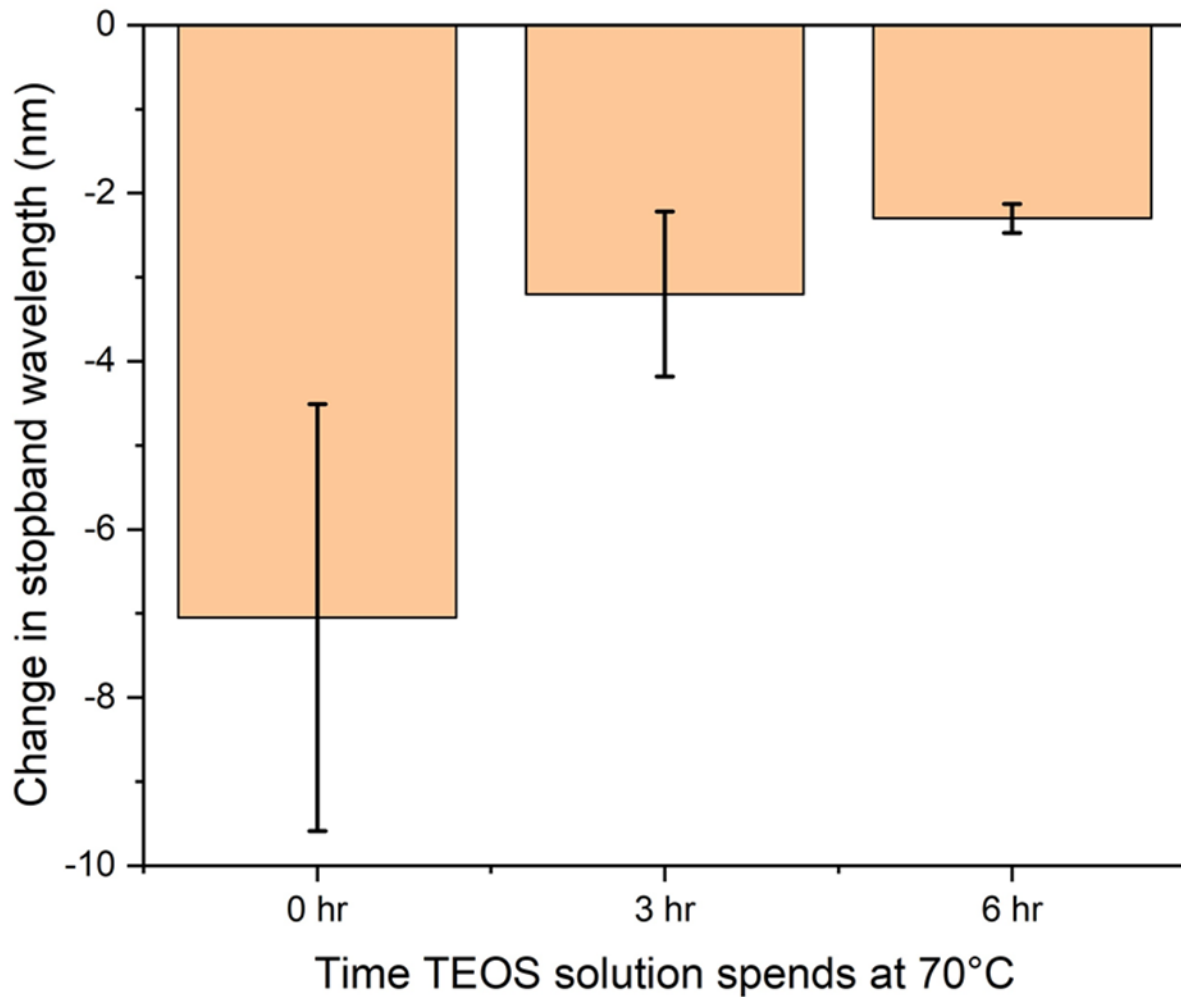


Figure 14. The effect of heating TEOS solution prior to inward-growing co-assembly on the change in stopband wavelength observed 3 weeks following fabrication. Using heat to induce some condensation of TEOS prior to co-assembly forms a silica network which is more resistant to shrinkage.

5.0 Silica Inverse Opal Diffraction Properties

5.1 Effects of Disorder

As mentioned in section 1.2, a major drawback to the vertical co-assembly method developed by our group was that the resulting IOs had very high baseline attenuation of deep UV light. This attenuation was believed to be diffuse scattering from the periodic surface inhomogeneities called striations. Since the scattering intensity is proportional to λ^{-4} , the intensity of the diffuse scattering from these striations sharply increased at smaller wavelengths. At the stopband center wavelength, nearly 80% of incident light was diffusely scattered (baseline extinction of ~ 0.7 OD) rather than Bragg diffracted at normal incidence. As a result, only $\sim 20\%$ of the incident light was Bragg diffracted by the vertically co-assembled IO. (Figure 15a)

Because inward-growing co-assembly does not result in surface striations, our IOs yielded much lower diffuse scattering baselines than those from vertically co-assembled IOs. From the baseline of the extinction spectrum, we observed that at the stopband center, as little as 20% of the incident light was diffusely scattered (extinction of 0.1 OD). For that sample, 50% of the incident light was Bragg diffracted. (Figure 15b) The intensity of the Bragg diffraction is comparable to that from the silica CCAs published by our group, with only slightly higher diffuse scattering baselines.¹³ This result represents a much more efficient Bragg diffraction than that of the vertical co-assembly method developed by our group.³

Notable is the fact that this intense Bragg diffraction resulted from an IO fabricated with 100 μL of PSNP/TEOS suspension rather than the usual 200 μL . This result was unexpected, as we believed that the intensity of Bragg diffraction would be directly proportional to the number of

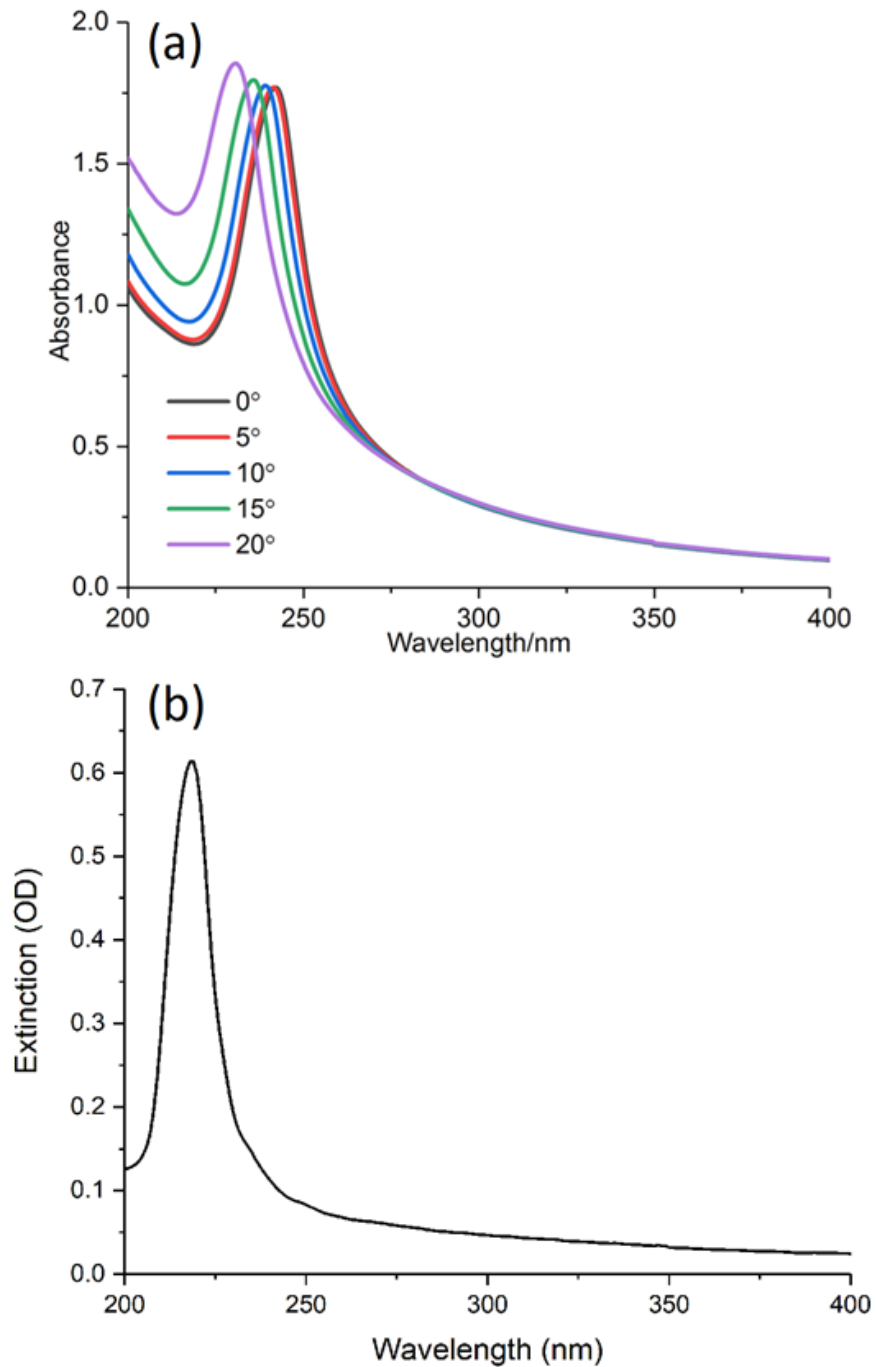


Figure 15. Comparison of extinction spectra of silica inverse opals fabricated by (a) vertical co-assembly and (b) inward-growing co-assembly. It is apparent that inward-growing co-assembly yields much lower diffuse scattering baselines, resulting in much more efficient Bragg diffraction. a reprinted with permission from Solid Deep Ultraviolet Diffracting Inverse Opal Photonic Crystals, K.T. Hufziger, A.B. Zrimsek, S.A. Asher, *ACS Appl. Nano Mater.* 2018, 1, 12, 7016-7024; DOI: [10.1021/acsanm.8b01806](https://doi.org/10.1021/acsanm.8b01806). Copyright 2018 American Chemical Society.

IO layers, and therefore the initial drop volume. However, based on the method of Bertone et al., we calculated that the critical silica IO thickness required to attenuate 50% of incident light would only be 7 layers.⁶⁴ Since the SEM micrographs in Figure 12 show nearly 30 IO layers formed with a 200 μL drop volume, one would expect much more light to be attenuated by that IO.

This finding led us to believe that the IO extinction more directly corresponded to the extent of order or disorder present in our IOs rather than the number of IO layers. With the lower 100 μL drop volume, fewer PSNPs were present to self-assemble, and therefore there were fewer possibilities for point and line defects with long-range structural effects in the IO. It also then makes sense that the diffuse scattering baseline and Bragg diffraction intensity are often not consistent across the entire IO, as they depend on local defects and disorder. This result helps rationalize the fact that, for vertical co-assembly, only certain regions of the IO strongly diffracted.³ In the case of inward-growing co-assembly, the strongly-diffracting region is the thin film covering most of the substrate between the coffee ring and the opaque region surrounding the void. With further optimization of the inward-growing co-assembly method, more consistent ordering with even more efficient Bragg diffraction could be achieved.

5.2 Diffraction Bandwidth

One performance characteristic that still hinders the use of the IO as a WSD is the diffraction bandwidth. The stopband of the strongly-diffracting IO in Figure 15b had a full width at half maximum (FWHM) of 15.0 nm as measured by an absorption spectrometer at normal incidence. For comparison, the CCA that our group previously demonstrated could be used as a WSD for a DUVRR spectrometer had a normal-incidence FWHM of 2.7 nm based on absorption

spectrometer measurements. Though normal-incidence extinction bandwidth measurements tend to overestimate the diffraction bandwidth,¹³ it is clear that the IO cannot select as narrow Raman shift ranges as the CCA.

A proposed method to decrease the bandwidth was to fill the air voids of the IO with a liquid to decrease the refractive index contrast between the silica network and the voids. As mentioned in section 1.1.1, the width of photonic stopbands is known to decrease with a decrease in refractive index contrast. Water, for example, has $n \sim 1.39$ in the deep UV,⁶⁵ a significant increase from that of air ($n = 1.00$). Therefore, filling the air voids with water would significantly reduce the refractive index contrast between the silica network and the voids. However, filling the voids would also increase the effective refractive index, increasing the stopband wavelength. Therefore, this experiment primarily served as proof of concept for this proposed method of bandwidth narrowing.

To determine the effect of filling the air voids of our IO with water, normal-incidence extinction spectra of the IO were recorded in air, in water, and in air again after drying. (Figure 16) After immersing the IO in water, the stopband wavelength increased from 228 nm to 301 nm, and the intensity reduced dramatically. Filling the IO voids with water did succeed at decreasing the bandwidth by nearly 50%, but at the cost of losing over 90% of the diffraction intensity. Clearly, for our IO, the losses in diffraction intensity make this method of narrowing the diffraction bandwidth impractical. Upon removing the IO from water and drying it completely, the stopband appears as it did before, showing that these stopband changes are reversible and depend only on the material in the IO voids.

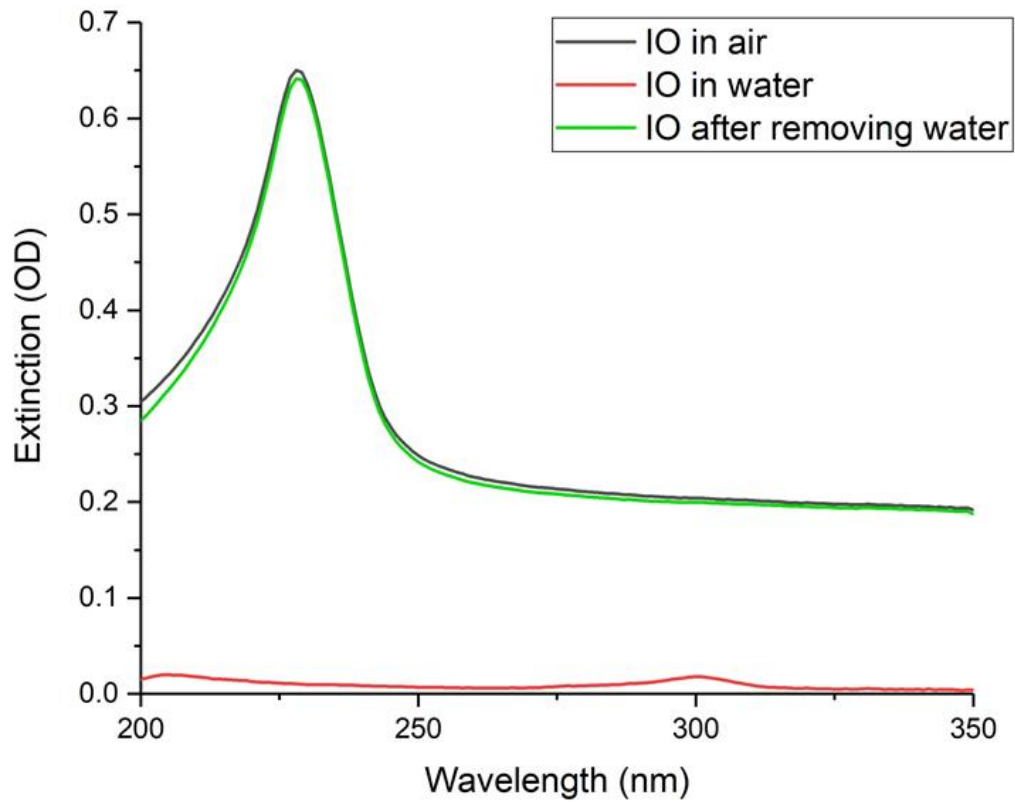


Figure 16. Normal-incidence extinction spectra of an IO in air (black), water (red), and after removing the water (green). The stopband red shifts by 73 nm upon filling the air voids with water, however almost all diffraction intensity is lost. This change is fully reversible, as after drying and evaporating the water, the stopband mirrors the original stopband.

6.0 Conclusions and Future Work

The diffraction properties of PhCs have shown to be promising for wavelength selection applications. Due to a lack of commercially-available deep UV optics, photonic crystals presented an opportunity to facilitate development of DUVRR spectrometers. The studies presented in this thesis sought to improve upon the existing CCA and IO technology pioneered by our group. We developed a novel method to co-assemble PSNPs with TEOS on horizontal substrates. Upon removing the PSNPs, a deep UV-diffracting silica IO remains attached to the substrate. This IO Bragg diffracts a maximum of 50% of incident deep UV light, while only diffusely scattering 20%. These diffraction properties represent major improvements upon the vertically co-assembled IOs published by our group.

Given the promise of this IO fabrication method, future work should focus on better optimizing these IOs for practical use. While we believed that our IOs would be indefinitely stable upon fabrication, we found that the IOs compressed along the normal over time, resulting in a blue shift in the stopband wavelength. Some work has been done to mitigate this compression, and should continue in the future. Also, while these IOs demonstrate Bragg diffraction intensity comparable to silica CCAs, the diffraction bandwidth is still significantly larger. As a result, the IO does not provide sufficient specificity to select Raman bands of particular explosives. Reducing the refractive index contrast by filling the air voids with a higher refractive index liquid is known to reduce the diffraction bandwidth, but also drastically reduces diffraction intensity. Increasing the number of diffracting layers, provided the layers are sufficiently well-ordered, could allow for greater diffraction intensity upon infilling with liquids. Additionally, fabricating the PS/SiO₂ PhCs using slightly larger PSNPs could result in more versatile IOs which are well suited for use with

multiple deep UV laser wavelengths (228 nm, 244 nm, 266 nm, etc.). Future improvements such as these could lead to a WSD that is optimal for use in a DUVRR spectrometer.

Appendix A Synthesis of PSNPs

We utilized a modified version of the Reese et al. emulsion polymerization procedure first described by Hufziger et al. to synthesize highly charged 143 ± 4 nm polystyrene nanoparticles. A custom 1 L jacketed cylindrical reactor (Ace Glass 6475-310, 4" ID with drain outlet) was fitted with a Teflon agitator (Ace Glass 8090-08 attached to a Teflon shaft) and attached to an overhead stirrer (Caframo BDC6015). A reflux condenser, a foil wrapped addition funnel, a long needle attached to an N₂ line, and a thermometer were also attached. The reactor temperature was controlled via an ethylene glycol bath recirculator (Thermo Neslab RTE 740). Styrene (Sigma Aldrich S4972, 99%) was passed through a column containing ~40g aluminum oxide (Aldrich 19974) to remove the butylcatechol inhibitor. 275.3 mL nanopure water (Barnstead Infinity) was added to the reactor. The stirring rate was set to 60 RPM, and then 0.3381 g sodium bicarbonate (NaHCO₃, JT Baker 3506-01) was added to the reactor. The reactor contents were deoxygenated for 15 min with N₂. 2.9501 g dihexyl sulfosuccinate sodium salt (Aldrich 86146, ~80% in H₂O, surfactant) was dissolved in 5.00 mL nanopure water and added to the reactor. The vial containing the surfactant was washed 3× with 5.00 mL aliquots (15 mL total) of nanopure water, adding each wash into the reactor to maximize surfactant transfer. The reaction mixture was deoxygenated with N₂ for an additional 20 minutes. 115.0 mL de-inhibited styrene was added to the addition funnel, and deoxygenated with N₂ for 30 minutes, followed by N₂ blanketing until the end of the reaction. During styrene deoxygenation, the stirring rate was set to 125 RPM, and reactor heating by the recirculator was initiated. When the reactor temperature reached ~50°C, the stir rate was set to 350 RPM and styrene was added at a rate of ~4 drops/sec (17 min total). 5 min. after the completion of styrene addition, 6.3513 g 3-allyloxy-2-hydroxy-1-propane sulfonic acid (Aldrich 409421,

~40% w/w in H₂O, co-monomer) was added to the reactor and the recirculator temperature setpoint was increased. When the reactor temperature reached 70.0 °C, 1.5029g ammonium persulfate ((NH₄)₂S₂O₈, Sigma Aldrich 248614, 98%, initiator) dissolved in 5.00 mL nanopure water was added to the reactor to initiate the reaction. After allowing the reaction to proceed for 2.0 hr, 1.0348 g additional co-monomer was added to the reactor, followed 2 min later by 0.9964 g additional (NH₄)₂S₂O₈ dissolved in 2.00 mL nanopure water. The reaction was allowed to proceed for 1.0 hr before being cooled while stirring. The cooled nanosphere dispersion was filtered through nylon mesh (Small Parts Inc., 120 μm). The dispersion was then poured into 14 kDa MWCO regenerated cellulose tubing (Sigma Aldrich D9402, soaked in nanopure water before use) and dialyzed against nanopure water for 6 weeks. The dispersion was then stored over mixed-bed ion-exchange resin (Bio-Rad AG-501-X8 (D), used as received).

Bibliography

1. Waterhouse, G. I.; Waterland, M. R., Opal and inverse opal photonic crystals: fabrication and characterization. *Polyhedron* **2007**, *26* (2), 356-368.
2. Míguez, H.; López, C.; Meseguer, F.; Blanco, A.; Vázquez, L.; Mayoral, R.; Ocaña, M.; Fornés, V.; Mifsud, A., Photonic crystal properties of packed submicrometric SiO₂ spheres. *Applied Physics Letters* **1997**, *71* (9), 1148-1150.
3. Hufziger, K. T.; Zrimsek, A. B.; Asher, S. A., Solid Deep Ultraviolet Diffracting Inverse Opal Photonic Crystals. *ACS Applied Nano Materials* **2018**, *1* (12), 7016-7024.
4. Yablonovitch, E., Inhibited spontaneous emission in solid-state physics and electronics. *Physical review letters* **1987**, *58* (20), 2059.
5. John, S., Strong localization of photons in certain disordered dielectric superlattices. *Physical review letters* **1987**, *58* (23), 2486.
6. Flaugh, P. L.; O'Donnell, S. E.; Asher, S. A., Development of a new optical wavelength rejection filter: demonstration of its utility in Raman spectroscopy. *Applied spectroscopy* **1984**, *38* (6), 847-850.
7. Asher, S. A.; Flaugh, P.; Washinger, G., 'Crystalline Colloidal Bragg Diffraction Devices: The Basis for a New Generation of Raman Instrumentation. *Spectroscopy* **1986**, *1* (12), 26-31.
8. Lee, K.; Asher, S. A., Photonic crystal chemical sensors: pH and ionic strength. *Journal of the American Chemical Society* **2000**, *122* (39), 9534-9537.

9. Asher, S. A.; Alexeev, V. L.; Goponenko, A. V.; Sharma, A. C.; Lednev, I. K.; Wilcox, C. S.; Finegold, D. N., Photonic crystal carbohydrate sensors: low ionic strength sugar sensing. *Journal of the American Chemical Society* **2003**, *125* (11), 3322-3329.
10. Holtz, J. H.; Asher, S. A., Polymerized colloidal crystal hydrogel films as intelligent chemical sensing materials. *Nature* **1997**, *389* (6653), 829.
11. Ward Muscatello, M. M.; Stunja, L. E.; Asher, S. A., Polymerized crystalline colloidal array sensing of high glucose concentrations. *Analytical chemistry* **2009**, *81* (12), 4978-4986.
12. Hufziger, K. T.; Bykov, S. V.; Asher, S. A., Raman hyperspectral imaging spectrometer utilizing crystalline colloidal array photonic crystal diffraction. *Applied spectroscopy* **2014**, *68* (11), 1219-1223.
13. Hufziger, K. T.; Bykov, S. V.; Asher, S. A., Ultraviolet Raman wide-field hyperspectral imaging spectrometer for standoff trace explosive detection. *Applied spectroscopy* **2017**, *71* (2), 173-185.
14. Geng, C.; Wei, T.; Wang, X.; Shen, D.; Hao, Z.; Yan, Q., Enhancement of light output power from LEDs based on monolayer colloidal crystal. *Small* **2014**, *10* (9), 1668-1686.
15. Mekis, A.; Chen, J.; Kurland, I.; Fan, S.; Villeneuve, P. R.; Joannopoulos, J., High transmission through sharp bends in photonic crystal waveguides. *Physical Review Letters* **1996**, *77* (18), 3787.
16. Lee, Y. J.; Braun, P. V., Tunable inverse opal hydrogel pH sensors. *Advanced Materials* **2003**, *15* (7-8), 563-566.
17. Barry, R. A.; Wiltzius, P., Humidity-sensing inverse opal hydrogels. *Langmuir* **2006**, *22* (3), 1369-1374.

18.Nakayama, D.; Takeoka, Y.; Watanabe, M.; Kataoka, K., Simple and precise preparation of a porous gel for a colorimetric glucose sensor by a templating technique. *Angewandte Chemie International Edition* **2003**, *42* (35), 4197-4200.

19.Vu, A.; Qian, Y.; Stein, A., Porous Electrode Materials for Lithium-Ion Batteries—How to Prepare Them and What Makes Them Special. *Advanced Energy Materials* **2012**, *2* (9), 1056-1085.

20.Long, J. W.; Dunn, B.; Rolison, D. R.; White, H. S., Three-dimensional battery architectures. *Chemical Reviews* **2004**, *104* (10), 4463-4492.

21.Osiak, M.; Geaney, H.; Armstrong, E.; O'Dwyer, C., Structuring materials for lithium-ion batteries: advancements in nanomaterial structure, composition, and defined assembly on cell performance. *Journal of Materials Chemistry A* **2014**, *2* (25), 9433-9460.

22.King, J. S.; Gaillot, D. P.; Graugnard, E.; Summers, C. J., Conformally Back-Filled, Non-close-packed Inverse-Opal Photonic Crystals. *Advanced Materials* **2006**, *18* (8), 1063-1067.

23.Bohn, J. J.; Ben-Moshe, M.; Tikhonov, A.; Qu, D.; Lamont, D. N.; Asher, S. A., Charge stabilized crystalline colloidal arrays as templates for fabrication of non-close-packed inverted photonic crystals. *Journal of colloid and interface science* **2010**, *344* (2), 298-307.

24.Li, Q.; Jonas, U.; Zhao, X.; Kappl, M., The forces at work in colloidal self-assembly: a review on fundamental interactions between colloidal particles. *Asia-Pacific Journal of Chemical Engineering* **2008**, *3* (3), 255-268.

25.Bolhuis, P. G.; Frenkel, D.; Mau, S.-C.; Huse, D. A., Entropy difference between crystal phases. *Nature* **1997**, *388* (6639), 235.

26.Yan, Q.; Zhou, Z.; Zhao, X., Inward-growing self-assembly of colloidal crystal films on horizontal substrates. *Langmuir* **2005**, *21* (7), 3158-3164.

27.Reculusa, S.; Ravaine, S., Synthesis of colloidal crystals of controllable thickness through the Langmuir– Blodgett technique. *Chemistry of materials* **2003**, *15* (2), 598-605.

28.Bardosova, M.; Pemble, M. E.; Povey, I. M.; Tredgold, R. H., The langmuir-blodgett approach to making colloidal photonic crystals from silica spheres. *Advanced materials* **2010**, *22* (29), 3104-3124.

29.Wijnhoven, J. E.; Vos, W. L., Preparation of photonic crystals made of air spheres in titania. *Science* **1998**, *281* (5378), 802-804.

30.Schroden, R. C.; Al-Daous, M.; Blanford, C. F.; Stein, A., Optical properties of inverse opal photonic crystals. *Chemistry of materials* **2002**, *14* (8), 3305-3315.

31.Mihi, A.; Ocaña, M.; Míguez, H., Oriented Colloidal-Crystal Thin Films by Spin-Coating Microspheres Dispersed in Volatile Media. *Advanced Materials* **2006**, *18* (17), 2244-2249.

32.Arcos, C.; Kumar, K.; González-Viñas, W.; Sirera, R.; Poduska, K. M.; Yethiraj, A., Orientationally correlated colloidal polycrystals without long-range positional order. *Physical Review E* **2008**, *77* (5), 050402.

33.Velev, O.; Jede, T.; Lobo, R.; Lenhoff, A., Porous silica via colloidal crystallization. *Nature* **1997**, *389* (6650), 447.

34.Holland, B. T.; Blanford, C. F.; Stein, A., Synthesis of macroporous minerals with highly ordered three-dimensional arrays of spheroidal voids. *Science* **1998**, *281* (5376), 538-540.

35.Ye, Y.-H.; LeBlanc, F.; Haché, A.; Truong, V.-V., Self-assembling three-dimensional colloidal photonic crystal structure with high crystalline quality. *Applied Physics Letters* **2001**, *78* (1), 52-54.

36.Zhou, Z.; Zhao, X., Opal and inverse opal fabricated with a flow-controlled vertical deposition method. *Langmuir* **2005**, *21* (10), 4717-4723.

37.Goldenberg, L. M.; Wagner, J.; Stumpe, J.; Paulke, B.-R.; Görnitz, E., Ordered arrays of large latex particles organized by vertical deposition. *Langmuir* **2002**, *18* (8), 3319-3323.

38.Yan, Q.; Gao, L.; Sharma, V.; Chiang, Y.-M.; Wong, C., Particle and substrate charge effects on colloidal self-assembly in a sessile drop. *Langmuir* **2008**, *24* (20), 11518-11522.

39.Nair, R. V.; Vijaya, R., Structural and optical characterization of photonic crystals synthesized using the inward growing self-assembling method. *Applied Physics A* **2008**, *90* (3), 559-563.

40.Gares, K. L.; Hufziger, K. T.; Bykov, S. V.; Asher, S. A., Review of explosive detection methodologies and the emergence of standoff deep UV resonance Raman. *Journal of Raman Spectroscopy* **2016**, *47* (1), 124-141.

41.Emmons, E. D.; Tripathi, A.; Guicheteau, J. A.; Fountain III, A. W.; Christesen, S. D., Ultraviolet resonance Raman spectroscopy of explosives in solution and the solid state. *The Journal of Physical Chemistry A* **2013**, *117* (20), 4158-4166.

42.Ghosh, M.; Wang, L.; Asher, S. A., Deep-ultraviolet resonance raman excitation profiles of NH₄NO₃, PETN, TNT, HMX, and RDX. *Applied spectroscopy* **2012**, *66* (9), 1013-1021.

43.Tuschel, D. D.; Mikhonin, A. V.; Lemoff, B. E.; Asher, S. A., Deep ultraviolet resonance Raman excitation enables explosives detection. *Applied spectroscopy* **2010**, *64* (4), 425-432.

44. Puppels, G.; Grond, M.; Greve, J., Direct imaging Raman microscope based on tunable wavelength excitation and narrow-band emission detection. *Applied spectroscopy* **1993**, *47* (8), 1256-1267.
45. Hatton, B.; Mishchenko, L.; Davis, S.; Sandhage, K. H.; Aizenberg, J., Assembly of large-area, highly ordered, crack-free inverse opal films. *Proceedings of the National Academy of Sciences* **2010**, *107* (23), 10354-10359.
46. Brinker, C. J., Hydrolysis and condensation of silicates: effects on structure. *Journal of Non-Crystalline Solids* **1988**, *100* (1-3), 31-50.
47. Thomson, N. R.; Bower, C. L.; McComb, D. W., Identification of mechanisms competing with self-assembly during directed colloidal deposition. *Journal of Materials Chemistry* **2008**, *18* (21), 2500-2505.
48. Teh, L.; Tan, N.; Wong, C.; Li, S., Growth imperfections in three-dimensional colloidal self-assembly. *Applied Physics A* **2005**, *81* (7), 1399-1404.
49. Deegan, R. D.; Bakajin, O.; Dupont, T. F.; Huber, G.; Nagel, S. R.; Witten, T. A., Capillary flow as the cause of ring stains from dried liquid drops. *Nature* **1997**, *389* (6653), 827.
50. Pallares, I. G.; Rout, D.; Deering, T. J.; Hufziger, K. T.; Bykov, S. V.; Asher, S. A., Colloidal Self-Assembly of Ordered Silica Inverse Opals for Deep Ultraviolet Diffraction. *ACS Applied Nano Materials* **Submitted**.
51. Buckley, A.; Greenblatt, M., The sol-gel preparation of silica gels. *Journal of chemical education* **1994**, *71* (7), 599.
52. Seu, K. J.; Pandey, A. P.; Haque, F.; Proctor, E. A.; Ribbe, A. E.; Hovis, J. S., Effect of surface treatment on diffusion and domain formation in supported lipid bilayers. *Biophysical journal* **2007**, *92* (7), 2445-2450.

53. Reese, C. E.; Guerrero, C. D.; Weissman, J. M.; Lee, K.; Asher, S. A., Synthesis of highly charged, monodisperse polystyrene colloidal particles for the fabrication of photonic crystals. *Journal of colloid and interface science* **2000**, *232* (1), 76-80.

54. Bohn, J. J.; Tikhonov, A.; Asher, S. A., Colloidal crystal growth monitored by Bragg diffraction interference fringes. *Journal of colloid and interface science* **2010**, *350* (2), 381-386.

55. Bordwell, F.; Algrim, D., Nitrogen acids. 1. Carboxamides and sulfonamides. *The Journal of Organic Chemistry* **1976**, *41* (14), 2507-2508.

56. Sulpizi, M.; Gaigeot, M.-P.; Sprik, M., The silica–water interface: how the silanols determine the surface acidity and modulate the water properties. *Journal of chemical theory and computation* **2012**, *8* (3), 1037-1047.

57. Yang, Y.; Jing, L.; Yu, X.; Yan, D.; Gao, M., Coating aqueous quantum dots with silica via reverse microemulsion method: toward size-controllable and robust fluorescent nanoparticles. *Chemistry of materials* **2007**, *19* (17), 4123-4128.

58. Phillips, K. R.; Vogel, N.; Hu, Y.; Kolle, M.; Perry, C. C.; Aizenberg, J., Tunable anisotropy in inverse opals and emerging optical properties. *Chemistry of Materials* **2014**, *26* (4), 1622-1628.

59. García, M. T.; Gracia, I.; Duque, G.; de Lucas, A.; Rodríguez, J. F., Study of the solubility and stability of polystyrene wastes in a dissolution recycling process. *Waste management* **2009**, *29* (6), 1814-1818.

60. Kazakevich, Y.; LoBrutto, R., *HPLC for pharmaceutical scientists*. Wiley Online Library: 2007; Vol. 43.

61. Sharp, J.; Forrest, J. A., Free surfaces cause reductions in the glass transition temperature of thin polystyrene films. *Physical review letters* **2003**, *91* (23), 235701.

62. Rodríguez-de Marcos, L. V.; Larruquert, J. I.; Méndez, J. A.; Aznárez, J. A., Self-consistent optical constants of SiO₂ and Ta₂O₅ films. *Optical Materials Express* **2016**, *6* (11), 3622-3637.

63. McDonagh, C.; Sheridan, F.; Butler, T.; MacCraith, B., Characterisation of sol-gel-derived silica films. *Journal of Non-Crystalline Solids* **1996**, *194* (1-2), 72-77.

64. Bertone, J. F.; Jiang, P.; Hwang, K. S.; Mittleman, D. M.; Colvin, V. L., Thickness dependence of the optical properties of ordered silica-air and air-polymer photonic crystals. *Physical Review Letters* **1999**, *83* (2), 300.

65. Daimon, M.; Masumura, A., Measurement of the refractive index of distilled water from the near-infrared region to the ultraviolet region. *Applied Optics* **2007**, *46* (18), 3811-3820.